4D-CT LUNG REGISTRATION AND ITS APPLICATION FOR LUNG RADIATION THERAPY

by

YUGANG MIN
B.S. Huazhong University of Science and Technology, 2000
M.S. University of Central Florida, 2005

A dissertation submitted in partial fulfillment of the requirements
for the degree of Doctor of Philosophy
in the Department of Electrical Engineering and Computer Science
in the College of Engineering and Computer Science
at the University of Central Florida
Orlando, Florida

Spring Term
2012

Major Professor: Sumanta N. Pattanaik
Co-advisor: Anand P. Santhanam

ABSTRACT

Radiation therapy has been successful in treating lung cancer patients, but its efficacy is limited by the inability to account for the respiratory motion during treatment planning and radiation dose delivery. Physics-based lung deformation models facilitate the motion computation of both tumor and local lung tissue during radiation therapy. In this dissertation, a novel method is discussed to accurately register 3D lungs across the respiratory phases from 4D-CT datasets, which facilitates the estimation of the volumetric lung deformation models. This method uses multi-level and multi-resolution optical flow registration coupled with thin plate splines (TPS), to address registration issue of inconsistent intensity across respiratory phases. It achieves higher accuracy as compared to multi-resolution optical flow registration and other commonly used registration methods. Results of validation show that the lung registration is computed with 3 mm Target Registration Error (TRE) and approximately 3 mm Inverse Consistency Error (ICE). This registration method is further implemented in GPU based real time dose delivery simulation to assist radiation therapy planning.

TABLE OF CONTENTS

LIST OF FIGURES

LIST OF TABLES

CHAPTER 1: INTRODUCTION

Cancer is one of the leading causes of death. National Vital Statistics Reports shows that in 2009 cancer accounted for more than 23% of total deaths in US, only second to heart disease in terms of mortality (Kochanek, Xu, Murphy, Minino, & Kung, 2011). Among all types of cancers, cancer in lung and bronchus is the second common diagnosed and the most deadly type of cancer for both men and women, as shown in Table 1 (American Cancer Society, 2010). Through efforts of tobacco control, the number of deaths by lung cancer has decreased in recent years. However, lung cancer still remains the No. 1 lethal causes among cancers.

Table 1: Leading sites of new cancer cases and death – 2010 estimates

2010 estimated new cases		2010 estimated deaths	
Male	Female	Male	Female
Prostate (28%)	Breast (28%)	Lung & bronchus (29%)	Lung & bronchus (26%)
Lung & bronchus (15%)	Lung & bronchus (14%)	Prostate (11%)	Breast (15%)
Colon & rectum (9%)	Colon & rectum (10%)	Colon & rectum (9%)	Colon & rectum (9%)

1.1 Lung Cancer and Treatments

From the perspective of clinical treatment, lung cancers are divided into small cell lung cancer and non-small cell lung cancer (NSCLC). Small cell lung cancer accounts for only 10% to 15% of all lung cancer cases, and NSCLC accounts for all the remaining cases (National Center for Health Statistics, 2011). In this dissertation the techniques we addressed are mainly related to NSCLC type of lung cancer.

Depending on the stage of the cancer, surgery, chemotherapy or radiation therapy may be used to treat NSCLC.

In stage I and stage II of lung cancer, most cancer cells stay locally together inside the lung and have not spread out beyond nearby lymph nodes yet, surgery treatment is preferred.

Lung cancer cells, when start to spread out, always invade into far away lymph nodes (stage III) and travel to the whole human body through lymphogenous channel (stage IV) (National Center for Health Statistics, 2011). In these stages, it is not possible to remove all tumors by surgery, chemotherapy and radiation therapy are used instead.

Chemotherapy delivers drugs in human body to kill fast growing cells or to stop these cells to proliferate. Since cancer cells grow much faster than most normal cells in human body, the drugs are well delivered to cancer cells, while surrounding normal cells remain safe. Unfortunately, certain cells in human body grow as fast as cancer cell (e.g. hair). Those fast growing healthy cells are damaged by chemotherapy as well. The patient can recover from such side effects after chemotherapy.

Chemotherapy is quite effective for stage III and stage IV of lung cancer, due to the fact that chemotherapy is administered orally or through intravenous or intramuscular injection, it gets through bloodstream then is distributed to the entire body.

Radiation therapy, on the other hand, only takes effect in a small section of human body. Radiation therapy uses external machine to deliver high energy x-rays or other type of radiation beams to a target area, to break DNA inside cells so that cells within the target area are killed. Radiation therapy cleans out small cancer cells that surgery cannot remove, but it also kills normal cells in the target area. Furthermore, research shows that patient receiving chest radiation

therapy are more likely to get cancer, as patient is under long term exposure to radiation (Anand, et al., 2008).

In order to effectively deliver dose while keep normal cells safe around the cancer area, various methods are used. Particularly for lung tumor the following methods are used:

- Improve tumor measurement accuracy: This method uses patient specific breathing model to locate the tumor, then control the radiation beam to shoot at the tumor only when it is in range during breathing.
- Use multiple low-energy radiation beams from different angles instead of using a single high-energy radiation beam to shoot tumor, so that the tumor receives a lethal amount of radiation dose while the surrounding healthy cells get only a small fraction of that radiation (Figure 1).

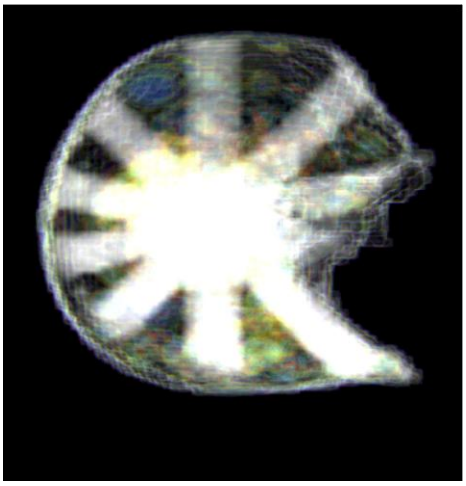

Figure 1: Multiple weak radiation beams shot at a tumor from different angles during radiation therapy planning simulation. (Min, Santhanam, Neelakkantan, Ruddy, Meeks, & Kupelian, 2010)

1.2 Clinical Body Scanning Techniques

Clinical experts evaluate radiation therapy plan before the treatment, for instance, the placement and strength of radiation beams to the lungs. Lung dynamics need to be counted for radiation dose delivery simulation during treatment planning. To obtain the lung dynamic information, 3D lung data need to be captured as the first step. The commonly clinical used body-scanning techniques are Ultrasound, MRI and CT.

Ultrasound clinical device sends and collects high frequency sound waves through human body. Using the different rate of penetrating ability of ultrasound through soft tissues, this method gets real-time images inside the human body. It does not utilize ionized radiation and hence is quite safe for patient body scanning. However, due to its poor performance through air pocket in the lungs, ultrasound is not a proper option for lung scanning.

Magnetic Resonance Imaging (MRI) is another safe scanning technique that does not emit ionized radiation. Magnetic field is used to align atomic nuclei in tissues, and then the tissues are exposed to a radio signal. Since such radio signal changes alignment of those atomic nuclei in tissues, by collecting radio frequency signal through the misaligned nuclei, detail images inside the human body can be generated. However, the long scanning time of MRI brings motion artifacts issue especially for lung scanning. In addition, the presence of air inside the lungs affects the MRI image contrast, thus the anatomical details that can be observed in MRI lung images are minimal.

CT, on the contrary, is a faster method to acquire 3D image. It uses several x-ray beam and sensor pairs that rotate helically around motorized table for multiple rounds, combines data from those rounds, and then reconstructs 3D data from the collected signals. For radiation

therapy, CT is used at two stages: (1) treatment planning, and (2) monitoring biological changes between treatment fractions. High-resolution CT images are required for the treatment planning stage. The tumor is defined in terms of Clinical Target Volume (CTV), which is the clinically delineated tumor volume, and Planned Target Volume (PTV), which is the tumor volume used for the radiation planning. Typically, PTV is larger than the CTV and includes a margin that accounts for patient setup variations and tumor motion during breathing. While there exists no specific study that quantifies the range of tumor motion, the margin is set to a generic value of 3 mm. CTV also helps in accounting for motion artifacts in the imaging system when the CT is acquired in the free breathing mode.

During the acquisition of High-resolution CT images, the human body or the lung region is exposed to high-energy radiation. For monitoring inter-fraction biological changes, it is a common practice to collect low-resolution data. The radiation dose in this case will be approximately 1.1 cGy per 3D scan, which compared to a 60 Gy lung radiotherapy treatment plan is negligible. The lower radiation dose leads to a lowered image quality and thus only the tumor region is tracked. The need to track both the tumor as well as the surrounding lung tissues is imminent.

1.3 4D-CT Registration for Lung Cancer Radiation Therapy

Technological developments in recent years have made CT scanners available for high-speed high-resolution clinical image that can be gated using a breathing surrogate. Thus multiple lung 3D volumes are acquired across respiratory phases during the imaging process. These scanners are known as 4D-CT scanners. The gated imaging provides opportunities for a more precise tumor volume acquisition. Recent 4D-CT scanners capture volumetric 3D lung data

using x-ray beams rotated in spiral manner, and hence captures slices of lungs for multiple breathing cycles with a lowered ionizing radiation. The gated 4D imaging enables accounting for lung motions that are not exactly the same during all breathing cycles.

The ability to acquire gated 4D-CT imaging opens the discussion of using a possible universal lung breathing motion model and use the captured slices at multiple breathing cycles to reconstruct geometry for a full breathing cycle. Structure of human lungs, such as bronchi and bronchial tree, has nearly the same distribution among people, but differ only by size. Assuming this physical similarity, it is natural to consider the possibility of using the same breathing motion model for all patients, and thus save on the time spent on CT scanning and data reconstruction for each individual. A universal lung breathing motion model can be considered in radiotherapy dose delivery planning for healthy people as healthy lungs have similar motions during breathing cycle. Unfortunately, such universal model cannot be used for most lung cancer patients. The reason is: the cancer changes the biological properties of the lung, and hence the lung surface expansions are no longer the same as normal people, and further, the breathing motion pattern of the patients are no longer the same. For instance, patients with NSCLC always breathe differently because the tissues affected by the tumors are no longer expandable, the tissues around the non-small cancer cells have to adapt to the rigid body inside the lung during breathing. Patients with other complications such as chronic obstructive pulmonary disease present shallow breathing.

Physics-based lung motion models may be developed to address the limitations to the lung radiotherapy. Physics-based model when modeled using precise parameters will exhibit a more accurate behavior. Physics-based lung models when developed using subject-specific

biomechanical properties and structural information can be coupled with breathing surrogates (which are also used for gated 4D-CT imaging) to monitor the lung motion during the radiation therapy. Such a monitoring capability opens the door to more advanced radiotherapy techniques such as adaptive radiotherapy, where the lung tumor is targeted as it moves during breathing. Additionally, the PTV margin can be reduced thereby sparing the radiation dose delivered to the tissues surrounding the tumor.

For developing such a physics-based model, it is important to reverse engineer the lung behavior that is exhibited by the subject and is acquired using the gated 4D-CT imaging. For such a reverse engineering process, a key requirement is to know how to register the different 3D volumes of the 4D-CT lung. When the lung is registered, the volumetric lung deformation is calculated, which illustrates, for any time during the patient's breathing cycle, how and where tumors and the surrounding tissues move, and plan the radiation dose delivery inside the lung. This dissertation focuses on 4D-CT registration techniques that solely enable the development of volumetric physics based lung models and subsequently the radiation dose delivery and monitoring.

Chapter 2 discusses the related work in the field of 4D-CT image registration. Rigid and non-rigid registration methods for the 4D-CT image registration are discussed and the non-rigid registration is championed. In particular, importance is given to optical flow based methods. A mathematical description of the optical flow method is discussed. The chapter concludes with a need to account for intensity variations for landmarks inside the lung.

Chapter 3 presents an analysis of the landmark intensity variation for a set of 4D-CT datasets. The analysis further quantifies the need to account for the landmark intensity variations in the 4D-CT.

Chapter 4 presents the proposed 4D-CT registration method that extends from the optical flow method and accounts for the landmark intensity variation. The description of the registration workflow is given.

Chapter 5 presents a validation study of the 4D-CT registration accuracy. For comparison purposes, 4 different registration methods with 2 segmentation options are considered. For analysis of the proposed system, variants of the proposed method are also discussed.

Chapter 6 presents the clinical importance of the proposed registration method in two steps. First, the development of a volumetric physics based lung model that uses the 4D lung deformation values computed from the optical flow based registration is discussed. Variations in the developed model caused by the use of 4D volumetric displacement computed from other registration methods are also discussed. Such a study shows the clinical relevance and importance of using the proposed registration paradigm. Second, the radiation dose documented by the proposed system is also discussed showing the clinical effect of inaccurate 4D-CT registration on the radiation dose documentation. Such a study in unique both in the field of radiation therapy and computer based image registration. The chapter concludes with a focus on 4D-CT registration accuracy on how it impacts the overall clinical workflow.

Chapter 7 concludes the dissertation with a discussion on the future possibilities of extending the proposed registration paradigm to other anatomical sites. A description of using the registration approach to head and neck anatomy is discussed. The dissertation concludes with

the need for more adaptive radiotherapy techniques for anatomical sites and the need for improved registration techniques where the focus on the registration accuracy is quantified based on its clinical implication and not just in a qualitative visualization.

CHAPTER 2: RELATED WORK

Lung dynamics is counted to achieve more accurate estimation in radiation dose delivery simulation for radiation therapy planning. The dynamics of the lung is computed by applying lung registration method on a sequence of 3D patient volume data captured from 4D-CT scanner. In this chapter, state-of-the-art lung registration techniques are investigated. Section 2.1 briefly describes various lung registration methods. Section 2.2 gives detailed information about optical flow lung registration technique, which is the type of lung registration used in the rest of the chapters.

2.1 Lung Registration

Rigid Body Transformations

Rigid-body transformations facilitate an automatic way of registering lungs from one air volume to another. The components of the rigid-body transformations include rotation, translation, scaling, and skewing. A simple way to mathematically explain the rigid-body transformation is as follows. Registering 3D lung volumes at different breathing volumes using a rigid-body transformation involves solving for the translation, rotation, scaling and skewing components. The method, being simple, assumes that the lung deformation during breathing is rigid, which is typically not the case when landmarks are tracked visually.

Thus, a rigid-body registration of the 3D lungs also aims at numerically minimizing the error involved in the registration of the lung volumes using optimization and convex

minimization techniques. The registration error, in this case, is the difference between the 3D target image and the 3D deformed source image. The literature on the minimization and optimization problem has been extensively investigated by peers and lies beyond the scope of this chapter (Tai, Lie, Chan, & Osher, 2005). Listed below are a few commonly used rigid body transformation techniques.

(Betke, Hong, & Ko, 2001) investigates an iterative rigid-body transformation–based approach for registering the lung surface models. The steps involved in this approach are as follows: first a set of landmarks with known correspondences was considered. These landmark points were then used to compute the rigid-body transformation components. The two steps were then repeated until the sum of the squared distances between the target image and the registration image is minimal. This method did not take into account the local continuity in displacement. Additionally, only the surface of the lung was registered. The method, however, accounted for changes in patient orientation.

(Hilsmann, et al., 2007) performs 4D-CT lung registration based on max inhale and max exhale CT images. The airway bifurcations were selected from vessel trees as landmarks. The corresponding feature points were tracked in the airways of two different volumes by using 3D shape context search. To keep the landmark correspondence search automatic, a unique 3D algorithm was developed in which, for each voxel in the vessel bifurcation, an additional value representing the local shape histogram was also considered. The correspondences were computed as a combination of both the voxel intensity as well as the histogram value. The rigid-body transformation was based on this landmark correspondence. This method was also iterative where the affine transformation is optimized using a least squares method.

(Betke M. , Hong, Thomas, Prince, & Ko, 2003) is based on intensity attenuation techniques, automatically chooses landmarks and performs landmark correspondences. This method chooses the landmarks in the sternum and vertebra areas, where the Hounsfield units (HU, a linear transformation of original attenuation coefficient measurement) are much larger than what was observed inside the lung and were significantly different from the soft tissue. As compared with (Hilsmann, et al., 2007), the landmarks in this case were outside the lungs. The center of the entire anatomical component on each 2D-CT slice of a 3D-CT scan set was taken as a landmark. Additionally, the trachea, in which the Hounsfield Unit (CT attenuation) values are much lower than –900, was also considered. The centers of each anatomy in each 2D slice were tracked from one volume to another. Now, the rigid-body transformation parameters were estimated for a given pair of source and target images. For known transformation parameters, the 3D lung volumes were then registered using the iterative closest-point method and Elias's nearest neighbor algorithm. In these steps, the translation vector and the rotation matrix of the rigid-body transformation were iteratively optimized until the sum of the squared distance between the correspondence obtained using the nearest neighbor algorithm and the iterative closest point is minimized.

This rigid-body registration method by (Blackall, Ahmad, Miquel, Landau, & Hawkes, 2004) is not limited to the CT imaging domain. It combines the breath-hold fast MRI with free-breathing MRI. Breath-hold MRI presents an improved shape representation for the 3D lungs. They are, however, in low resolution and low contrast as compared with the free-breathing MRI because of increased acquisition time. A registration of the breath-hold MRI with free-breathing MRI enables a prediction of the closest lung air volume that represents free breathing. Two

groups of fast MRI, a breath-hold multi-position MRI and a sequence of dynamic free-breathing MRI are registered using rigid-body transformations. Landmarks in this case were picked from the exhalation breath-hold MRI. Voxel similarity, which represents the voxel intensity difference as well as the local shape description, was used for finding the initial correspondences, and the rigid-body transformation parameters were then solved.

B-Splines and Thin-Plate Splines

4D-CT lung registration can be accommodated with the application of splines. Mathematically, splines are higher order polynomials whose coefficients or control points determine the shape of the curve. Splines are fundamentally one-dimensional in nature. They can, however, be extended into 2D and 3D by using a combination of more than one spline for each additional dimension. Since its inception, splines have been used for 2D registration extensively. It is beyond the scope of this chapter to explain in detail how a spline works and its 2D application. However, 4D-CT lung registration has benefited significantly from two particular types of splines, B-splines and thin-plate splines (TPS).

B-splines are third-order polynomials in which the control points determine the shape of the 3D object being represented. For any given 3D segmented lung, the B-splines naturally represent the contours of the lung shape and can be scaled to include the entire lung anatomy. Thus, for a given lung, the B-spline is generated by solving for the control points using simultaneous linear equation-solving techniques. From a registration perspective, for any two given lung CT data sets, their corresponding B-spline models can be generated by solving for the control points of each of the models. Once the control points are known, a registration of the control points from one lung volume to another will register the lung contours of one volume to

another. Optionally, the correspondence between the control points of one volume to another can also be done semi-automatically by a clinical expert for better accuracy. The method is also computationally faster because for any given lung, the number of control points is of the order of quarter of the set of voxels that define the lung (Farin, 1987).

(Murphy, van Ginneken, Pluim, Klein, & Staring, 2008) uses multi-resolution B-splines. Specifically, the distribution of the landmarks inside the lungs was divided into four regions for each lung. Multi-resolution data for each lung are created and an expert tracked the landmark motion on each resolution. The rest of the lung was registered using B-splines. The accuracy of the landmarks was then studied. Additionally, the inter-observer difference is shown to be at least 2 mm. Variations in the accuracy were shown as a function of the number of resolutions used and the number of steps involved in the stochastic gradient descent method.

In the approach of (McClelland, et al., 2006), several CT slabs were scanned during patient free-breathing CT (FBCT), each slab consisting of 20 to 30 volumes. FBCT has a fast scanning rate; however, it yields relatively low-quality volume data. A higher quality, breath-holding CT scan was then performed as a reference volume. The high-quality scan has thinner slices and a higher resolution, resulting in less noise and more detail in the volume. For gating purposes, the breathing level was determined by two methods: by assessing the volume that was computed from extracted surfaces or by locating the markers attached on the patient chest that are located by stereo camera. Each slab of volume data was then registered to the reference volume by 3D cubic B-spline non-rigid fitting. Two levels of resolution were applied on grid control points. The motion model for each slab was built by temporal fitting of all the registrations. The motion model for the whole lung was constructed by merging the models of all

the slabs together. Some discontinuities were observed near the slab boundaries and were validated by visually checking the difference between the predicted volume and the actual volume. The results were evaluated for tumor region, ipsilateral lung, and other tissues. Validation was also applied by point tracking—one landmark was picked in each slab and reference volume by a clinical oncologist, then the difference between the manually picked ones and the ones in the motion model are compared.

TPS are second-order polynomials in which the control points lie on the curve generated and also determine the shape of the 3D lung being represented. The advantage of the control points being part of the contour is that the landmarks, generated manually or automatically and registered can be used for the registration. A simple walkthrough of TPS based lung registration follows: for a given lung, the TPS control points are first solved as previously discussed for B-splines. Once the TPS model is generated for a given pair of lungs, the control points can then be manually or automatically registered. This step is easier compared with B-splines because the control points do not lie on the contour. Once the correspondences of the control points are known, the lungs are then subsequently registered using the spline function.

(Klinder, Lorenz, von Berg, Renisch, Blaffert, & Ostermann, 2008) discusses an effort to register the breath-hold CT, which is a precursor to the 4D-CT imaging. The imaging process involved the patient holding his/her breath at the start of breathing and at the end of breathing. The end-expiration and end-inspiration CT of the lungs were used for estimating the 3D lung motion. 3DCT volume data are captured as inhale–exhale breath-holding thorax CT images. The lung surface was extracted from the model and then covered with a topologically identical surface mesh for both surfaces. A sparse motion field was constructed by tracking corresponding

points on the mesh. A dense motion field was computed from such a sparse motion field by TPS interpolation. TPS, in a 2D case, was similar to the bending force of a thin metal surface. To apply TPS in 2D coordinate transformation, the bending force between the **x**-axis and the **y**-axis is the displacement of that node along these axes. A lung surface mesh was generated by performing a connected-component algorithm on selected threshold images from reference inhale–exhale volumes. Mesh adaptation was performed iteratively.

Physics-Based 3D Warping and Registration from Lung Images

One of the earliest approaches for performing 4D-CT lung registration is using physics based 3D lung warping techniques (Fan & Chen, 1999). In this approach, a few landmarks, namely, the airway bifurcations, were tracked from one volume to another. The surrounding anatomy was registered from one volume to another using a continuum mechanics approach. A continuum mechanics model was applied to CT images for nonlinear interpolation with the assumption that the CT image intensity was equivalent to mass density. Three main constraints were used: noncompressibility, divergent free, and continuity preserving. The combination of these three constraints makes the registration math similar to computational fluid dynamics. An anisotropic smoothness filter was applied to maintain the local continuity of the displacement.

The following relation mathematically explains noncompressibility. Let f represent the spatial description of the 3D lung volume indexed by t. The noncompressibility relation states that the spatial description f is equal to the negative product of the spatial description of the estimated velocity and the gradient of the spatial description itself. As such, the lung anatomy consists of a combination of solid and liquid substances whose densities vary. To assume noncompressibility, the spatial density was assumed to be a constant.

The divergent-free constraint states that the divergence of the velocity, which represents the local expansion or contraction of the air, must be zero for regions where the spatial descriptor f is nonzero. Such divergent-free constraints are more commonly used in solving fluid flow problems using computational fluid dynamic techniques. It is to be noted that from a lung biology perspective, the air temperature changes when it flows through the lungs, so the whole volume of air in the lung changes as well.

Continuity preserving is typically accounted by considering isotropic smoothness constraint. This constraint aims at minimizing the summation of the square of displacements along each direction. However, in this study, the authors have used an anisotropic smoothness constraint by using a weighted value for each direction. Such an approach facilitated motion continuity when the local gray scale differences were large. Of particular importance in the case of lungs is the case where we encounter breathing air coupled with liquid and solid anatomical substances, which causes the lung to move differently from each other. As an alternative, Lame's constants were used for continuity preserving (Vik, et al., 2008). In the case of lungs, the imaging data typically had a higher slice thickness (resolution along the z-axis) than the anatomical landmarks involved. For instance, a given landmark can appear on one slice of a 3D volume and not appear on the other slice of another 3D volume of the same lung. Thus, considering physics-based constraints for registration will compensate for the accuracy of the registration. In conclusion, the continuity-preserving aspect of the registration is the only applicable aspect of the registration. Nevertheless, physics-based registration methods offer a mathematical compact registration system that enforces the continuity of the registration. However, care needs to be given to the applicability of the physics not only from a biology

perspective but also from the perspective of imaging limitations.

Inverse Consistent Registration

The consistency of an image registration approach is a mutual information–based approach (Rangarajan, H., & Duncan, 1999), in which the registration algorithm is able to obtain the same result when a source image is registered to the target image and when the target image is registered to the source image. When the registration algorithm is unable to uniquely describe the correspondences between two images, the algorithm is deemed inconsistent. The inverse consistent registration aims at maximizing the consistency of a registration by minimizing the registration differences between the source-to-target and target-to-source correspondences. To further explain the method, let us consider the rigid-body transformation. Let S and T be the source and target lung volume, respectively. The rotation, translation, scaling, and skewing components of the rigid-body transformation are required to be inverted when T is registered to S instead of S to T. The key point to observe is that the underlying math in the rigid-body transformation does not guarantee consistency. Adding consistency to the registration method requires minimizing the differences between the transformations between the S to T and T to S registrations. It is now straightforward to include this constraint to the already iterative methods of solving for rigid-body transformations.

TPS can be combined with the inverse consistency constraint (Johnson & Christensen, 2002). Specifically, for TPS to be used for registration, the landmark correspondences are first computed either manually or automatically. Once computed, the TPS function uses the landmark correspondences to compute the correspondences for all the voxels in the 3D volume. A simpler way to achieve consistency is to first formulate a cost function that aims at minimizing the

bending energy to avoid large displacements and minimizing the displacement differences between the forward and reverse transforms. From a cost function minimization perspective, whenever there is a function with two independent terms to minimize, a third perturbation term that updates the other two terms in a heuristic manner is introduced. By applying this logic, a third TPS-based perturbation term was used to update both the forward and the reverse TPS transformation functions to minimize the difference between the displacements.

Inverse consistency can be used in combination with physics-based constraints (Johnson & Christensen, 2001). Instead of a semiautomatic approach to compute landmark correspondence, a manual way to register landmarks from one airway tree to another was used. It was followed by a cost minimization function that, when used, will give the registration of all the other points. The cost minimization included both linear elasticity constraints and reverse displacement constraints. The latter can be explained as follows. First, the displacement of source A to target B was computed. Then the displacement from source B to target A was computed. Now two different aspects are taken into account: first, the difference between the voxel distribution of the source and the target; second, the difference between the displacement of each voxel when computed using the forward and the reverse manner. The strength of this approach lies in the stability of the algorithm provided by the inverse consistency itself. The method, however, assumed a constant elastic parameter during registration, which is typically not the case.

In another approach, the small lung deformation is included as a constraint during registration (Christensen, Song, Lu, El, & Low, 2007). Tidal breathing (free breathing) volume CT data are collected, followed by the application of a small deformation inverse that is

consistent with the linear elastic (SICLE) registration to construct the motion field. The cost function of SICLE was presented as a weighted sum of imaging modality, bending energy, and inverse consistency. The application of such a registration has been used for the estimation of the lung tissue expansion and tissue mechanics. The key parameter observed from the 4D-CT registration was computed as a Jacobian value, which is the second-order curl of the local gradient. Although the tissue expansion can be obtained from xenon CT imaging, the inverse consistency also helped in obtaining a stable registration while registering multimodal image registration. Additionally, the Jacobian parameter helped in quantifying the lung tissue expansion and contraction.

Optical flow registration is another category for lung registration. As our registration method is based on optical flow, we will discuss this category in great detail.

2.2 Optical Flow Methods

The registration textures inside the lung (e.g. tumors, air pockets, tracheas and blood vessels) move along with the lung during patient breathing. The motion of the lung can be estimated by register the textures across respiratory phases. Optical flow registration is a method to use the entire textures field to find voxel correspondence, and minimize the overall motion variation between neighborhood voxels. Therefore, if the estimated displacement of an air pocket is different from estimated displacement of trachea region next to it, the two will compromise displacement with each other, so that the overall displacement difference is minimized.

Optical flow registration was first developed for rigid body motion estimation scenario in 2D, later on was expanded to 3D.

Fundamental Explanation of 2D Optical Flow Registration

Optical flow registration assumes that object intensity remains the same during the motion. Therefore,

$$I(x, y, t) = I(x + \delta x, y + \delta y, t + \delta t) \tag{2.1}$$

I stands for intensity. Since optical flow registration also assumes the displacement to be small, the relation of displaced location to the original location is unveiled by applying Taylor Series Expansion:

$$I(x + \delta x, y + \delta y, t + \delta t) = I(x, y, t) + \frac{\partial I}{\partial x}\delta x + \frac{\partial I}{\partial y}\delta y + \frac{\partial I}{\partial t}\delta t + H.O.T. \tag{2.2}$$

By ignoring higher order terms (H.O.T.), according to Equation 2.1,

$$\frac{\partial I}{\partial x}\delta x + \frac{\partial I}{\partial y}\delta y + \frac{\partial I}{\partial t}\delta t = 0 \tag{2.3}$$

Divide by δt on both sides of the Equation 2.3:

$$I_x u + I_y v + I_t = 0 \tag{2.4}$$

I_x, I_y and I_t in Equation 2.4 stand for the partial derivative of intensity along *x*, *y* and *t* (time dimension) separately, *u* and *v* is optical flow vector. At this point, there are two unknown variables *u* and *v* but only one equation. This leads to motion ambiguity (as known as "aperture problem") with insufficient number of equations as constraints.

Many approaches have been proposed to solve motion ambiguity by adding more constraints to the image differential equation. The most wildly used are Lucas-Kanade method and Horn-Schunck method.

The Lucas-Kanade Method

Lucas-Kanade method (Lucas & Kanade, 1981) assumes the same motion for all nearby pixels. By this assumption, Equation 2.3 is true for $I(x, y, t)$ and all the pixels around it. Therefore,

$$\begin{gathered} I_{x1}u + I_{y1}v + I_{t1} = 0 \\ I_{x2}u + I_{y2}v + I_{t2} = 0 \\ \vdots \\ I_{x(n-1)}u + I_{y(n-1)}v + I_{t(n-1)} = 0 \\ I_{xn}u + I_{yn}v + I_{tn} = 0 \end{gathered} \tag{2.5}$$

n is the number of pixels around the pixel of interest. The n equations are more than enough to solve the motion.

The equations can be written as

$$\begin{bmatrix} I_{x1} & I_{y1} \\ I_{x2} & I_{y2} \\ \vdots & \vdots \\ I_{x(n-1)} & I_{y(n-1)} \\ I_{xn} & I_{yn} \end{bmatrix} \begin{bmatrix} u \\ v \end{bmatrix} = - \begin{bmatrix} I_{t1} \\ I_{t2} \\ \vdots \\ I_{t(n-1)} \\ I_{tn} \end{bmatrix} \tag{2.6}$$

It can be transformed to

$$\begin{bmatrix} I_{x1}I_{x2}\cdots I_{x(n-1)}I_{xn} \\ I_{y1}I_{y2}\cdots I_{y(n-1)}I_{yn} \end{bmatrix} \begin{bmatrix} I_{x1} & I_{y1} \\ I_{x2} & I_{y2} \\ \vdots & \vdots \\ I_{x(n-1)} & I_{y(n-1)} \\ I_{xn} & I_{yn} \end{bmatrix} \begin{bmatrix} u \\ v \end{bmatrix} = - \begin{bmatrix} I_{x1}I_{x2}\cdots I_{x(n-1)}I_{xn} \\ I_{y1}I_{y2}\cdots I_{y(n-1)}I_{yn} \end{bmatrix} \begin{bmatrix} I_{t1} \\ I_{t2} \\ \vdots \\ I_{t(n-1)} \\ I_{tn} \end{bmatrix}$$

Then

$$\begin{bmatrix} u \\ v \end{bmatrix} = \begin{bmatrix} \sum_{i=1}^{n} I_{xi}^2 & \sum_{i=1}^{n} I_{xi}I_{yi} \\ \sum_{i=1}^{n} I_{xi}I_{yi} & \sum_{i=1}^{n} I_{yi}^2 \end{bmatrix} \begin{bmatrix} -\sum_{i=1}^{n} I_{xi}I_{ti} \\ -\sum_{i=1}^{n} I_{yi}I_{ti} \end{bmatrix} \tag{2.7}$$

Since the assumption that motions around pixel of interest are the same is always not true, modification has been made to more precisely reflect the real scenario by associating the Euclidean distance to the pixel of interest as a weight to the gradient of each pixel. So the closest pixels have greater impact to determine the motion, while pixels far away have lesser impact to the flow vector of the pixel of interest.

As the spatial and temporal differential of each pixel can be computed in parallel, Lucas-Kanade method has an advantage in computation efficiency. It is much easier to implement Lucas-Kanade method on GPU.

The Horn-Schunck Method

Horn-Schunck method (Horn & Schunck, 1981) does not strictly require nearby pixels share the same motion. However, it assumes global smoothness. In other words, motions of neighborhood pixels are as similar as possible.

Horn-Schunck method places an extra constraint to Equation 2.4 to solve optical flow motion by minimizing energy function

$$E = \iint [(I_x u + I_y v + I_t)^2 + \alpha^2(|\nabla u|^2 + |\nabla v|^2)]dxdy \tag{2.8}$$

The second part of the function is a smoothness term. α^2 adjusts the weight of the smoothness in the global energy function. This function can be minimized with Euler-Lagrange equations. Giving *L* as the integrand function of the global energy function *E*,

$$\frac{\partial L}{\partial u} - \frac{\partial}{\partial x}\frac{\partial L}{\partial u_x} - \frac{\partial}{\partial y}\frac{\partial L}{\partial u_y} = 0$$

$$\frac{\partial L}{\partial v} - \frac{\partial}{\partial x}\frac{\partial L}{\partial v_x} - \frac{\partial}{\partial y}\frac{\partial L}{\partial v_y} = 0$$

So,

$$I_x(I_x u + I_y v + I_t) - \alpha^2 \Delta u = 0$$

$$I_y(I_x u + I_y v + I_t) - \alpha^2 \Delta v = 0 \quad (2.9)$$

Δ is Laplacian operator. $\Delta u(x, y)$ can be approximated as $\bar{u}(x, y) - u(x, y)$, similarly, $\Delta v(x, y)$ can be approximated as $\bar{v}(x, y) - v(x, y)$. $\bar{u}$ and $\bar{v}$ are weighted average velocity of neighborhood pixels. Bring such approximations to the equations above,

$$I_x^2 u + I_x I_y v + I_x I_t + \alpha^2 u - \alpha^2 \bar{u} = 0$$

$$I_x I_y u + I_y^2 v + I_y I_t + \alpha^2 v - \alpha^2 \bar{v} = 0$$

Therefore,

$$u = \frac{(I_y^2 + \alpha^2)\bar{u} - I_x I_y \bar{v} - I_x I_t}{I_x^2 + I_y^2 + \alpha^2}$$

$$v = \frac{(I_x^2 + \alpha^2)\bar{v} - I_x I_y \bar{u} - I_y I_t}{I_x^2 + I_y^2 + \alpha^2}$$

(2.10)

Since the value of $\bar{u}$ and $\bar{v}$ depend on the value of *u* and *v*, which is not available at the very beginning, initial values are given to the motion field. From the initial values, $\bar{u}$ and $\bar{v}$ are computed as weighted average of *u* and *v*, and then *u* and *v* are updated as shown in Equation 2.11. Later, the value of $\bar{u}$ and $\bar{v}$ are updated as weighted average of *u* and *v*, so on and so forth.

$$\bar{u}^k = \sum_{i=1}^{n} a_i u_i^k$$

$$\bar{v}^k = \sum_{i=1}^{n} a_i v_i^k$$

$$u^{k+1} = \frac{(I_y^2 + \alpha^2)\bar{u}^k - I_x I_y \bar{v}^k - I_x I_t}{I_x^2 + I_y^2 + \alpha^2}$$

$$v^{k+1} = \frac{(I_x^2 + \alpha^2)\bar{v}^k - I_x I_y \bar{u}^k - I_y I_t}{I_x^2 + I_y^2 + \alpha^2}$$

(2.11)

In Equation 2.11, a_i is weight of nearby pixel to the pixel of interest. Velocity gets updated until convergence or until maximum number of iterations has been reached. Initial velocity u^0 and v^0 have great impact to the convergence speed and accuracy. The final velocity tends to lean on the direction where initial velocity orientation is set, so the result space is highly influenced from the initial velocity value. To be simple, the initial value of velocity u^0 and v^0 are set to zero, so $\bar{u}^0$ and $\bar{v}^0$ are zero as well.

Horn-Schunck method can achieve dense motion vectors, as the inner region of moving object will get motion from boundaries during iterations. However, it is not robust to noise. This issue will be further discussed in Chapter 3.

Comparing to Lucas-Kanade method discussed earlier, Horn-Schunck method is more suitable for lung registration, as lung deforms during breathing, which violates Lucas-Kanade method assumption that nearby pixels have the same velocity. The elasticity property of the lung makes the velocity transition from one point to its neighbor point smooth. For this reason, the Multi-Level Multi-Resolution optical flow method for lung registration discussed in Chapter 4 is based on Horn-Schunck method.

3D Optical Flow for Lung CT Image Registration

Although 3D optical flow registration has been used in computer vision for a long time, (Guerrero, Zhang, Huang, & Lin, 2004) is the first one to introduce 3D optical flow registration technique to lung registration in 2004. 2D optical flow method can be extended to 3D optical flow by adding extra dimension component,

$$I_x u + I_y v + I_z w + I_t = 0$$

And equations in Horn-Schunck method are modified to

$$u^{k+1} = \frac{(I_y^2 + I_z^2 + \alpha^2)\bar{u}^k - I_x I_y \bar{v}^k - I_x I_z \bar{w}^k - I_x I_t}{I_x^2 + I_y^2 + I_z^2 + \alpha^2}$$

$$v^{k+1} = \frac{(I_x^2 + I_z^2 + \alpha^2)\bar{v}^k - I_x I_y \bar{u}^k - I_y I_z \bar{w}^k - I_y I_t}{I_x^2 + I_y^2 + I_z^2 + \alpha^2}$$

$$w^{k+1} = \frac{(I_x^2 + I_y^2 + \alpha^2)\bar{w}^k - I_x I_z \bar{u}^k - I_y I_z \bar{v}^k - I_z I_t}{I_x^2 + I_y^2 + I_z^2 + \alpha^2}$$

(2.12)

In 2D optical flow method the spatial resolution along x dimension and y dimension are the same. When the method is extended to 3D, spatial resolution along depth dimension is usually lower than the other two dimensions due to 4D-CT scanner hardware limitation. For instance, spatial resolution along x and y dimension are approximately 0.97mm per voxel, while resolution along z dimension is approximately 3mm per voxel.

When optical flow technique that originally developed for rigid body registration is applied to patient lung CT volume data registration, some issues come up. In general, optical flow method deals with rigid opaque objects. The lung is different in the following: (1) The lung is elastic. (2) The intensity of CT volume slices is not lighting reflection from surface as in

general rigid body registration scenario, it is an accumulative scattered x-ray value through a slice of moving tissue. (3) The lung density changes, as air inhaled and exhaled from the lung during patient breathing cycles. Therefore, for the same spot on the lung, the intensity is not likely to be the same during the motion. (Guerrero, et al., 2006) accounts for variations in the intensity of landmarks from one volume to another by introducing an error function that is assumed to be small.

Multi-Resolution 3D Optical Flow Registration

Image intensity differential based optical flow registration methods, such as Lucas-Kanade method and Horn-Schunck method, assume small motion between origin data and target data, so that Taylor Series Expansion used in Equation 2.2 can be valid. Such assumption is not always true in real-world applications. (Zhang, et al., 2008) concludes that the displacement of more than 1 voxel in 3D space cannot be accurately registered without any modification of classical optical flow registration method. To address this issue, multi-resolution approach is applied to classical optical flow registration. It resizes data to smaller scale, so that the same pixel distance can represent larger displacement, as shown in Figure 2.

In other words, large displacements in real world coordinates become smaller in image space coordinates by applying multi-resolution rescaling, so that optical flow method can register the displacement accurately. Figure 3 demonstrates how it works in a 1D example. Displacement of 2.9 mm in real world coordinate is about 3 pixels away in image coordinate, which is beyond the capability of classical optical flow method for accurate registration. By rescaling the displacement by a factor of 2, it becomes 1.5 pixels away. If apply the rescaling again, the displacement reduces to 0.8 pixels, which falls into the range that optical flow method can

register accurately. After the displacement gets registered, the displacement is expanded and carried to the next resolution level. It keeps doing this way until it reaches the original scale.

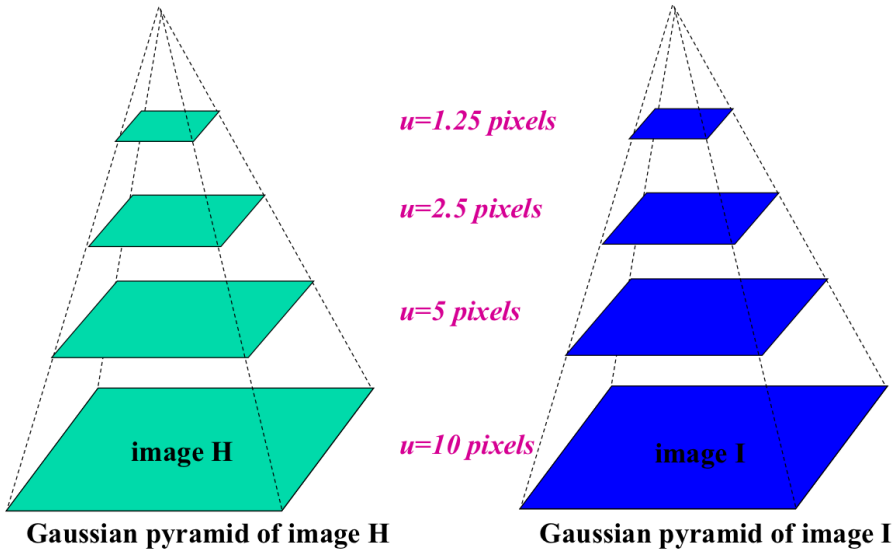

Figure 2: Multi-resolution optical flow method applied on a pair of images.

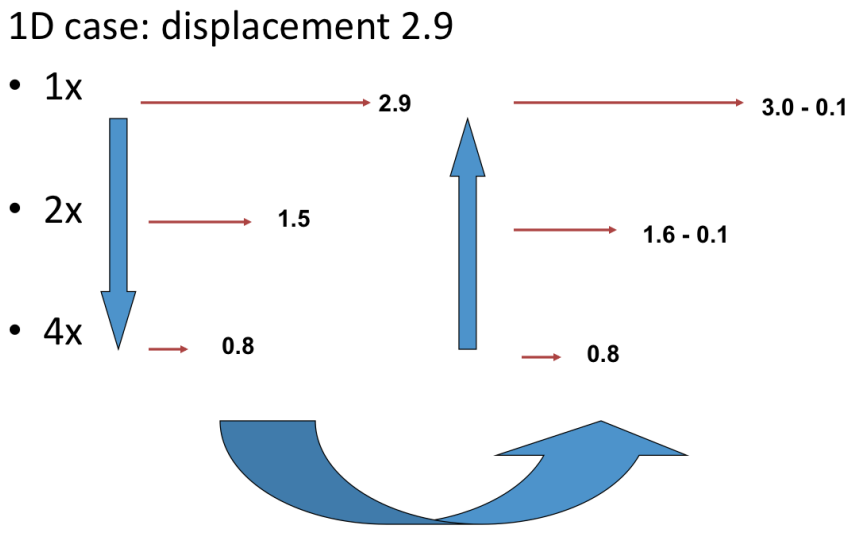

Figure 3: 1D example of multi-resolution registration

Inverse Consistent 3D Optical Flow Registration

Theoretically, giving a pair of lung volume A and B, registration from volume A to volume B and registration from volume B to volume A may be considered to be exactly the opposite. However, it is always not true. Inverse consistent method (Yang, Li, Low, Deasy, & Naqa, 2008) gives adjustment in pass-by-pass manner during registration iterations, so that the registration differences from volume A to B and that from volume B to A can be within certain threshold.

Dense Optical Flow

Intensity constancy issue in intravascular ultrasound (IVUS) image optical flow registration has been addressed in (Danilouchkine, Mastik, & van der Steen, 2009). This paper argues that from the ultrasound scattering aspect, intensity constancy in IVUS images does not hold, but the overall energy preserves. This paper derives modified optical flow registration for IVUS images based on an extra constrain of continuum mechanics conservation laws, which is called “dense optical flow”.

2.3 Summary

In real-world radiation therapies, due to high radiation exposure to patient during 4D-CT scanning, the scanning time is quite limited. And since 4D data reconstruction requires data to be captured in high speed, volume data obtained from 4D-CT scanner are in relatively low resolution and noisy. Such patient data doesn’t work well with optical flow based registration process, because optical flow registration method locates corresponding point from one frame to another frame based on the intensity or gradient similarity.

To enhance 4D-CT lung data registration, two modifications are provided. In Chapter 3 we introduce an innovate method to address intensity constancy issue, which extracts geometry feature in region of interest (ROI) from lung 4D-CT data and then mandatorily unify those feature intensities. In Chapter 4 we will discuss multiple anatomy level segmentation. With both intensity unification and multiple-anatomical-level segmentation applied, the optical flow registration performance with noisy 4D-CT data is evaluated in Chapter 5.

CHAPTER 3: LANDMARK INTENSITY VARIATION

Optical flow based registration method was originally developed for rigid body object tracking. The scenario of lung registration by optical flow method is different. In the context of 4D-CT volume data, intensity is defined as the accumulated radiation through a slice of human body non-rigid tissues. First of all, the sequence of 3D volume data is reconstructed from multiple x-ray 2D projections around patient body, the light source rotate around the object in high speed, instead of steady lighting direction in classic optical flow tracking scenario; Second, the lung density changes, as the air volume inside the patient's lung changes along with the inhale and exhale process; Third, instead of rigid, lung deforms during breathing, leads to the change of the accumulated radiation value through the deformed lung (the x-ray 2D projection). Because of these, for the same landmarks inside the lung, the intensity in corresponding respiratory phases are not the same.

In this chapter, we provide our observation of the intensity changes in 4D-CT patient data, then we give a 4D-CT data preprocess method to solve the issue so optical flow method can be used to accurately register the 4D-CT dataset.

3.1 Intensity Variation

60 landmarks are marked by clinical experts on each of the ten respiratory phases of HR 4D-CT. For brevity, five of the landmarks and their variation in each of the respiratory phases are shown in Figure 4. In each of the graphs, the vertical legend represents the Hounsfield Unit

(HU) value while the horizontal legend represents the respiratory phase index. It can be seen that while the five landmarks have relatively the same range of intensity values, the landmarks do not show any correlation in their intensity values. In addition, there is no correlation between variation and breathing patterns. Such variation of HU value brings error to the registration process.

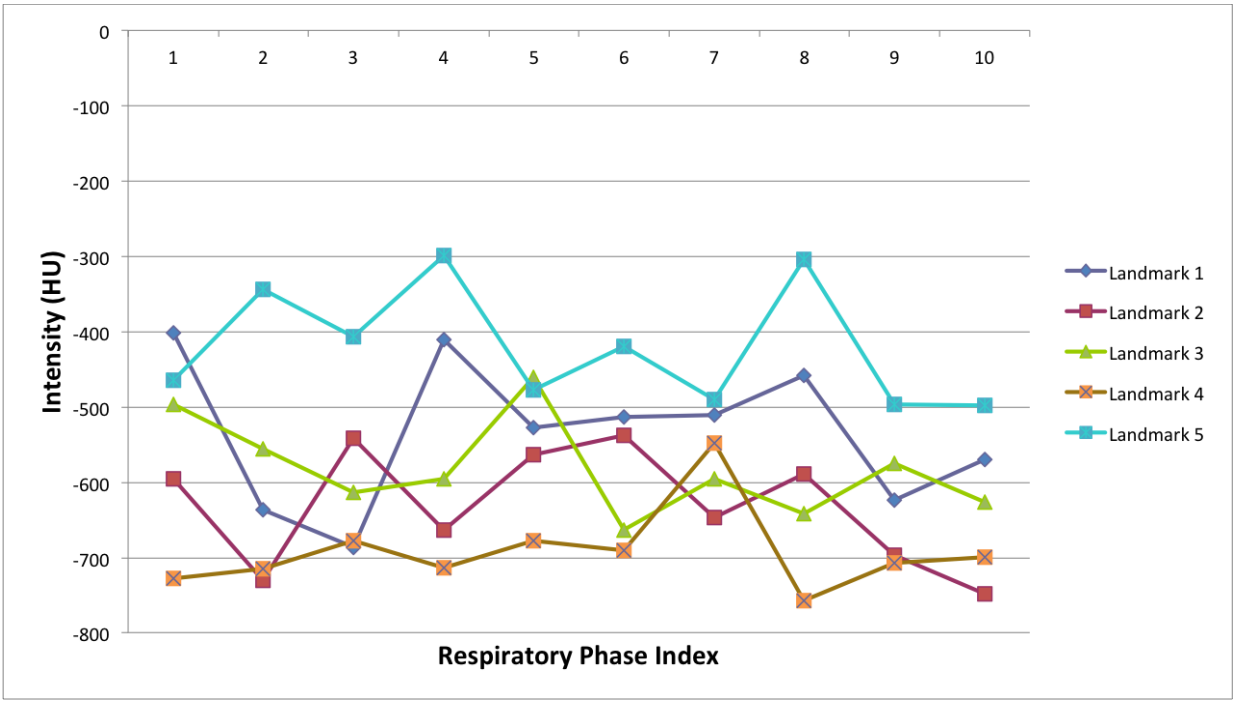

Figure 4: Landmark intensity variations for landmarks in the left and right lung

This analysis showed that, to obtain an accurate image-based registration of 4D-CT lungs with optical flow method, the data needs to be conditioned in such a way that the HU values of all anatomical features inside the lung be constant across the respiratory phases. In this dissertation, multiple anatomical levels are used to improve displacement estimation accuracy for voxels that intensity changes. We segment a 3D-CT lung data at multiple anatomical levels

based on the anatomy features, and then assign the same HU value to all the feature points on that anatomical level.

3.2 Intensity Unification Method

Landmarks inside the lung can be any feature pattern such as a spot on a tumor, a lymph node, a blood vessel knot, etc. All the landmarks visually stand out from the surrounding tissues. As section 3.1 points out, landmark HU value changes from phase to phase, and the intensity gradient may not remain the same, but there is one feature doesn't change – large intensity gap over its neighbors. If thresholds are properly set, voxels with similar HU values are grouped together, and then all voxels in the same range can be assigned to a given value. By this intensity unification process, optical flow registration method is likely to find the same intensity of the landmark from one phase to another. We setup a synthetic 2D scenario of two perpendicular blood vessels in dark parenchyma region (Figure 5) to demonstrate how the intensity unification process solves the intensity variation issue. The bottom part of Figure 5(a) numerically presents the intensity of the two blood vessels varies from the first phase to the second. Note that the intensity of parenchyma area also varies. Despite of the intensity changes, we can still clearly recognize the two blood vessels from the dark parenchyma region. We setup an intensity threshold of 60 – any voxel with intensity higher than 60 are in blood vessel area, otherwise that voxel belongs to parenchyma region. With the two types of anatomy, we apply intensity unification to the two anatomy levels: 150 to blood vessel level, 20 to parenchyma level, as shown in Figure 5(b). By applying intensity unification on different anatomy levels, voxels on blood vessel in the first phase will has counterpart voxels on blood vessel in the second phase.

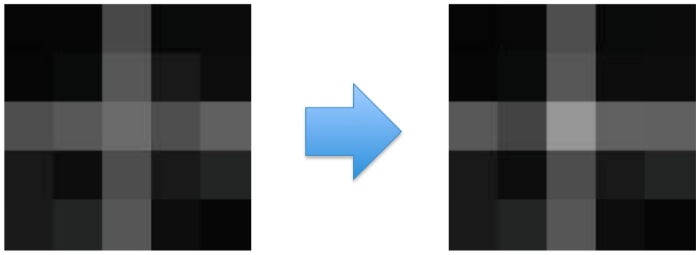

12	14	75	16	18
13	17	89	30	20
80	90	109	80	98
30	20	79	30	40
32	40	88	20	14

12	15	80	16	18
13	17	89	20	20
90	70	150	99	98
30	20	79	30	40
32	40	88	20	14

(a)

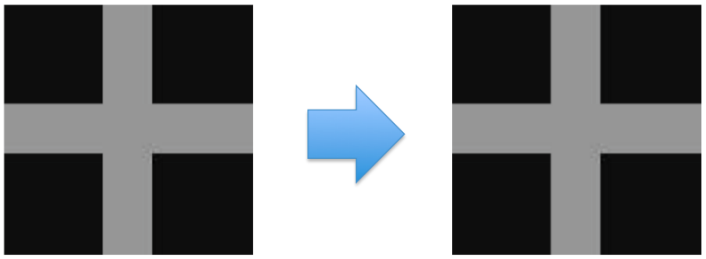

20	20	150	20	20
20	20	150	20	20
150	150	150	150	150
20	20	150	20	20
20	20	150	20	20

20	20	150	20	20
20	20	150	20	20
150	150	150	150	150
20	20	150	20	20
20	20	150	20	20

(b)

Figure 5: Intensity unification process on a pair of 2D synthetic images. (a) Before intensity unification process; (b) After intensity unification process.

Intensity unification method has been applied into the Multi-Level Multi-Resolution (MLMR) optical flow based lung registration. Instead of using a single threshold as shown in the

example given in this chapter, several thresholds are set to preserve more intensity details such as lung surface contours, blood vessels, etc.

Intensity unification is the first step of the MLMR method. It helps to increase registration accuracy. The detail of applying intensity unification into each anatomical level of the lung will be discussed in Chapter 4, the registration validation and comparison with other methods will be discussed in Chapter 5.

CHAPTER 4: MULTI-LEVEL MULTI-RESOLUTION APPROACH

The issue of intensity variation for lung registration is addressed in this dissertation by Multi-Level Multi-Resolution approach. This chapter will discuss why and how the lung are segmented into multiple anatomy levels for optical flow registration, and how we implement MLMR optical flow method to register a pair of 3D lung volume.

4.1 Multiple Anatomy Level Segmentation

Segmenting lung into multiple anatomy levels has several advantages:

- Facilitate intensity unification process, as discussed in Chapter 3. Our optical flow method first register surface contour only, and then register blood vessels with surface contour, and then register the whole lung. With the intensity unified on the anatomy levels, our registration method has no intensity variation issue.
- Improve registration accuracy. We modified weighted sum of nearby displacement component in our optical flow registration method, so that contribution from low contrast region is discarded, while contribution from high contrast region is preserved. The anatomy level of the voxel is used as indicator to tell if a voxel nearby is in relatively high contrast region. If the voxel belongs to higher or equal anatomy levels, we consider it as from high contrast region.

3D Lung Segmentation

The multi-level lung anatomy in our approach is segmented into surface contour, blood vessels and parenchyma regions. The blood vessel region is further segmented into multiple levels according to user specification.

Lung surface contour is the easiest among the categories to be tracked due to relatively sharp contrast of the lung to the surrounding tissue. The great amount of blood inside blood vessels projects bright lines in CT slices makes it stand out from the dark parenchyma regions.

The blood vessel region is segmented using two different approaches. In the first approach, intensity thresholds are investigated, and then all the voxels are automatically assigned the anatomy levels according to the HU value. Figure 6 illustrates four anatomy levels (Blood vessel region is further segmented into 2 levels). The large and small blood vessels are segmented using this automatic method. Every successive level includes the anatomy of its previous level.

The second approach, a semi-automatic seed-based region growth method is investigated to obtain the blood vessel morphology. The locations of one or more seeds representing the blood vessels were selected on each respiratory phase of a 4D-CT dataset. The voxel belongs to blood vessel or not is determined by the HU value difference between that voxel and seed, and whether there is connectivity between the voxel and the blood vessel region.

For our implementation, we developed an interface to manually place seeds on all of the respiratory phases for registration convenience (Figure 7). Placing a single seed may find only a portion of the whole blood vessel network, this utility helps user to select a proper location to add seed (the red dot on Figure 7(a)) to find more blood vessels. Slices from all phases are

displayed together, HU value of each newly placed seed is also shown underneath the slice, to help user to select the seed to similar places across all the phases.

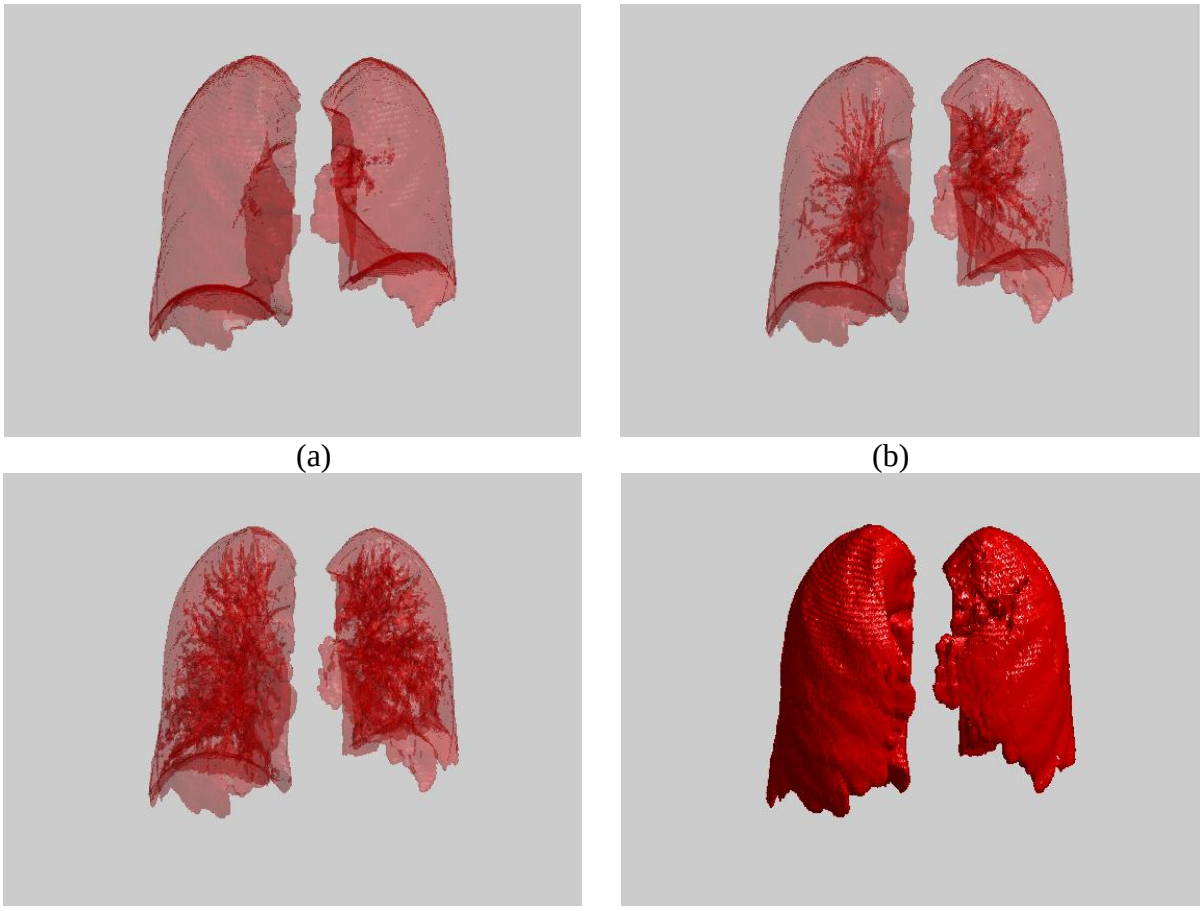

(a) (b)

(c) (d)

Figure 6: The lung at different anatomical levels. (a) Surface contour only (b) Surface contour and large blood vessels (c) Surface contour, large and small blood vessels (d) the whole lung including parenchyma regions.

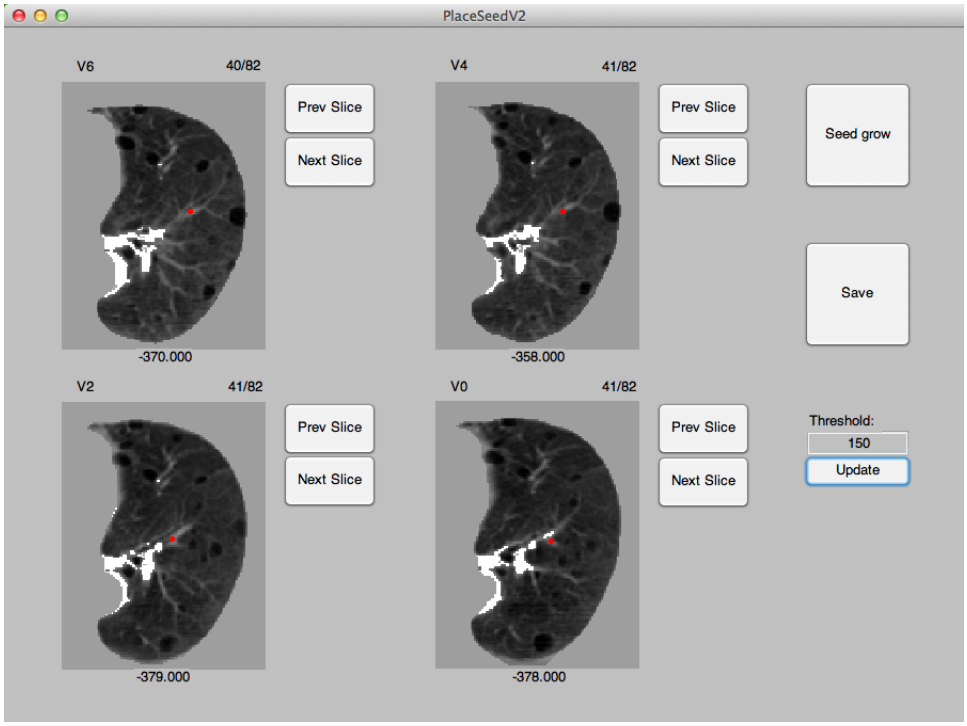

(a)

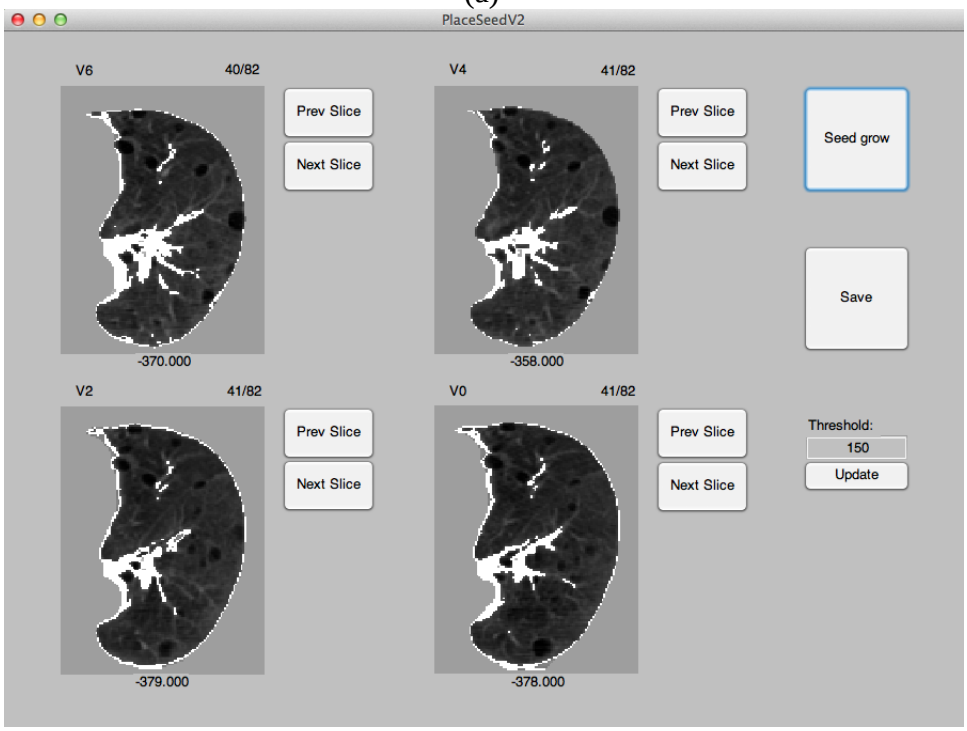

(b)

Figure 7: Interface for seed-based region growth segmentation method. (a) Seed (the red dot) is placed to find more blood vessels; (b) The newly found blood vessels are added to the blood vessel trees.

Modified Weighted Sum of Neighborhood Displacement

In classical optical flow registration method, displacement of a point is estimated by computing weighted sum of displacements from all nearby points (Equation 2.12). When implement optical flow method on lung registration, we observe that registration error is higher in low intensity contrast region (such as parenchyma area) than that in high intensity contrast area, such as lung surface contour. Discarding the weighted sum contribution from low intensity contrast region improves registration accuracy. Our modified weighted sum of neighborhood displacement counts in points only from region with higher or equal intensity contrast. We use the anatomy level of the neighborhood voxels to tell the relative intensity contrast. If the voxel nearby has lower anatomy level, we set the weight to be 0 (discard weighted sum contribution); if the voxel nearby has higher or equal anatomy level, we count in the weighted sum contribution, as shown in Figure 8. Diamonds are voxels from lower anatomy levels, triangles are the nearby voxels with higher or same anatomy levels.

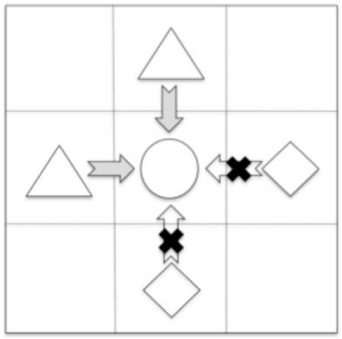

Figure 8: Displacement estimation by modified weighted sum of neighborhood voxels.

Note that other than parenchyma region, the rest three anatomy categories sparsely distributed in lung volume. Although contain the same intensity, blood vessels and surface

contour corresponding counterpart in the other volume can still be located by their unique 3D geometry patterns.

4.2 Multiple Resolution

The proposed optical flow registration method applies a combination of multiple anatomy level and multiple volume resolution based registration coupled with thin plate splines (TPS).

Due to the fact that optical flow registration method only works well in small displacements scenario, multi-resolution applies to deal with large displacements (Zhang, et al., 2008). In lower resolution volumes, the same amount of displacements is represented in closer voxel distances, so that optical flow registration method performs well. The computed displacements are then expanded to higher resolution level to get original displacement. Multi-resolution is used to increase accuracy of registering voxel pair faraway; multiple anatomy level method, on the other hand, improves displacement estimation accuracy locally, especially if neighborhood voxels have low contrast ratio (e.g. parenchymal region).

Because of the large displacement during lung breathing, multi-resolution is applied first, and then the pair of surface contour volume, the pair of large blood vessel volume, the pair of small blood vessel volume, and the pair of whole lung volume is rescaled to half size for each resolution level. In the proposed method, we normally apply 6 levels of resolution. Thus, the bottom resolution level contains the original size volume data; top resolution level stores volume that is only 1/32 of the original volume size.

4.3 Thin Plate Spline

Starting from top resolution level, volume pair of first anatomy level (surface contour) is registered, then TPS is introduced to facilitate the displacement at current anatomy level to be propagated to the volume at the next anatomy level as initial displacement. It is to be noted that for an iterative registration algorithm such as the optical flow, the accuracy of the final results strongly depends on the initial value of the displacement. In our proposed work, the smoothing constraint is not only for the final result but also for the initial displacement values for the subsequent level of registration. TPS facilitate the displacement computed from one level of anatomy to be propagated to the volume at the next level of anatomy as initial displacement. It is to be noted that the optical flow's smoothness constraint is different from the proposed TPS usage. The final registration is an iterative combination of the multiple anatomical levels and resolutions coupled with TPS, which is one of the key contributions of the dissertation.

4.4 MLMR Registration Setup and Implementation

The MLMR optical flow registration system is implemented in OSX 10.6. Patient data are a series of 3D volumes captured from 4D-CT scanner.

Firstly, grow region tool in OsiriX is used to segment the lungs from the surrounding tissues. The segmented lung are exported slice by slice in text image format. Then for each lung slice text image, contour maps are created by outline tool in ImageJ. Contour is the first anatomical level of the lung for the proposed MLMR registration method. To segment blood vessels, we use both automatic (intensity thresholds) and semi-automatic (seed based region growth) methods, for comparison of registration performance, as mentioned in section 4.1. For automatic segmentation, a MATLAB script segments the rest anatomical levels, including large

blood vessels and small blood vessels, on each slice based on normalized intensity value. For instance, all the points having intensity above 180 and not contour belong to large blood vessels; while all the points having intensity between 180 and 100 are small blood vessels; the rest are parenchyma regions. For semi-automatic segmentation, we use the seed placement interface that we developed to place multiple seeds on each of the 3D lung to be registered, let the program to find the blood vessel network.

The main part of MLMR registration is implemented on MATLAB. The set of 3D lung volume pairs (the pair of surface contour, the pair of large blood vessel volumes, the pair of small blood vessel volumes and the pair of the whole original volume) are loaded. As shown in Figure 9, 3D volumes of each anatomy level are scaled down to the lowest resolution. Surface contour (the first anatomy level) is the first to be registered by optical flow method. At this moment, all the voxel displacements except those on the surface contour are zeros. TPS smoothing applies to the displacement volume so that voxels next to the surface contour get a good initial displacement value close to the ground-truth displacement. The displacement volume is computed, applied by TPS and then carried to the next anatomy level until it reaches the fourth anatomy level (parenchyma regions). At this step, the two phases are registered in the lowest resolution level. Displacement values are doubled and carried to the higher resolution levels as initial displacement volume, then continue phase registration as the process above, until the original resolution volume registration is completed. At this point, the displacement volume contains the final registration result from the MLMR method.

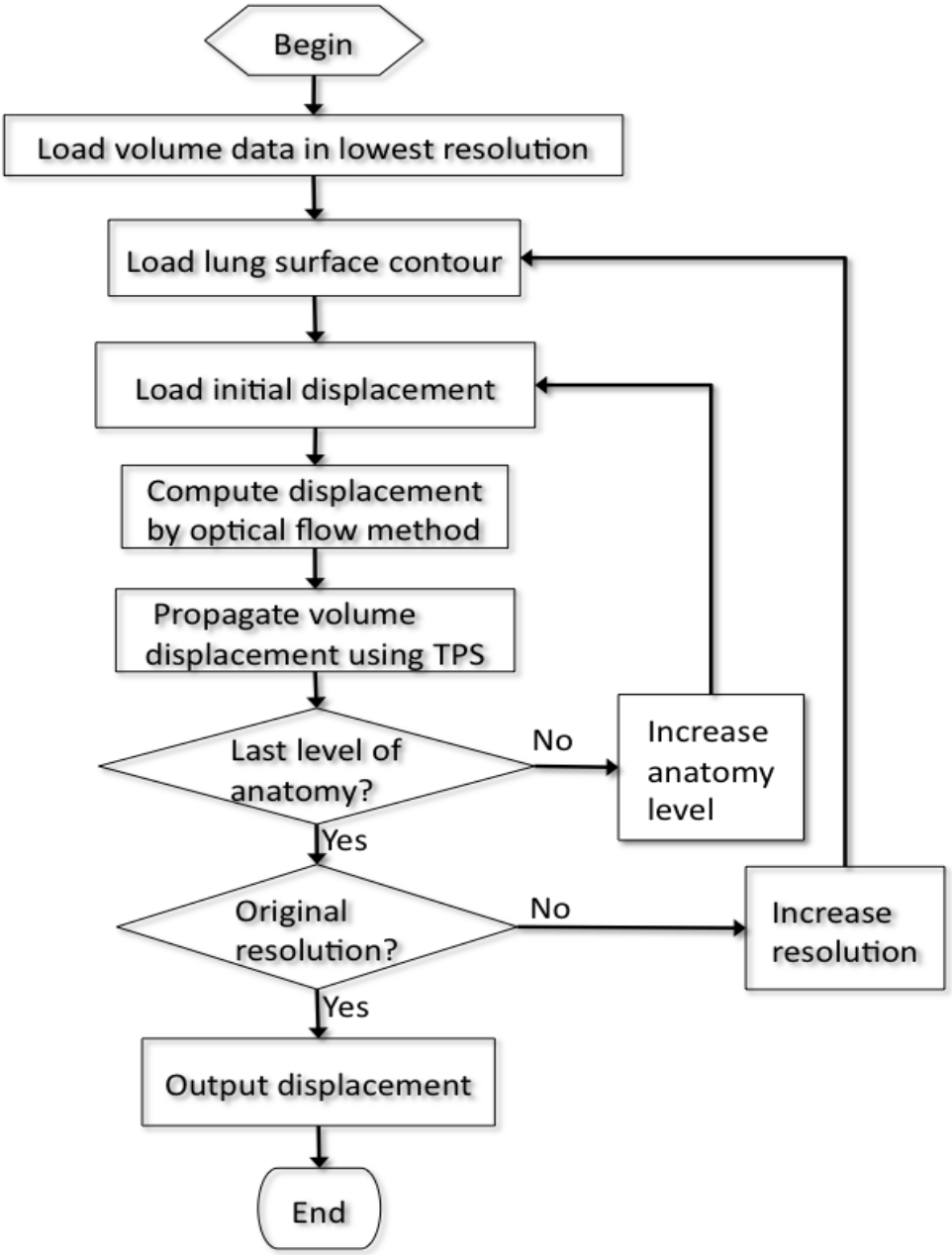

Figure 9: Multi-Level Multi-Resolution registration method flowchart.

4.5 Summary

Together with intensity unification and multi-anatomical-level segmentation, we modified classical optical flow registration method to fit the noisy non-rigid 4D-CT lung data

registration scenario. Registration analysis using this method will be discussed and compared with other lung registration methods in Chapter 5.

CHAPTER 5: RESULTS VALIDATION AND ANALYSIS

The MLMR optical flow registration method is developed to register 4D-CT lung volumes, especially to address the intensity variation issue. This chapter will analyze the performance by comparing with some other registration methods. Multiple set of parameters are used in our MLMR method in the comparison study.

5.1 Lung Displacement Result Visualization

Figure 10 illustrates the displacement magnitude of each anatomical level at each of the three directions. For consistency, the same CT slice index is chosen for all the images. The displacement vectors of the surface contours are computed followed by the large and small vessels and finally the parenchyma region. The results from one level of anatomy are propagated to the next level of anatomy using TPS (Figure 10(a)-(d)). For the parenchyma region, the displacement is computed using the TPS alone. For comparison purposes, the displacement computed using the multi-resolution optical flow is shown (Figure 10(e), which differs from the displacement computed using the MLMR approach.

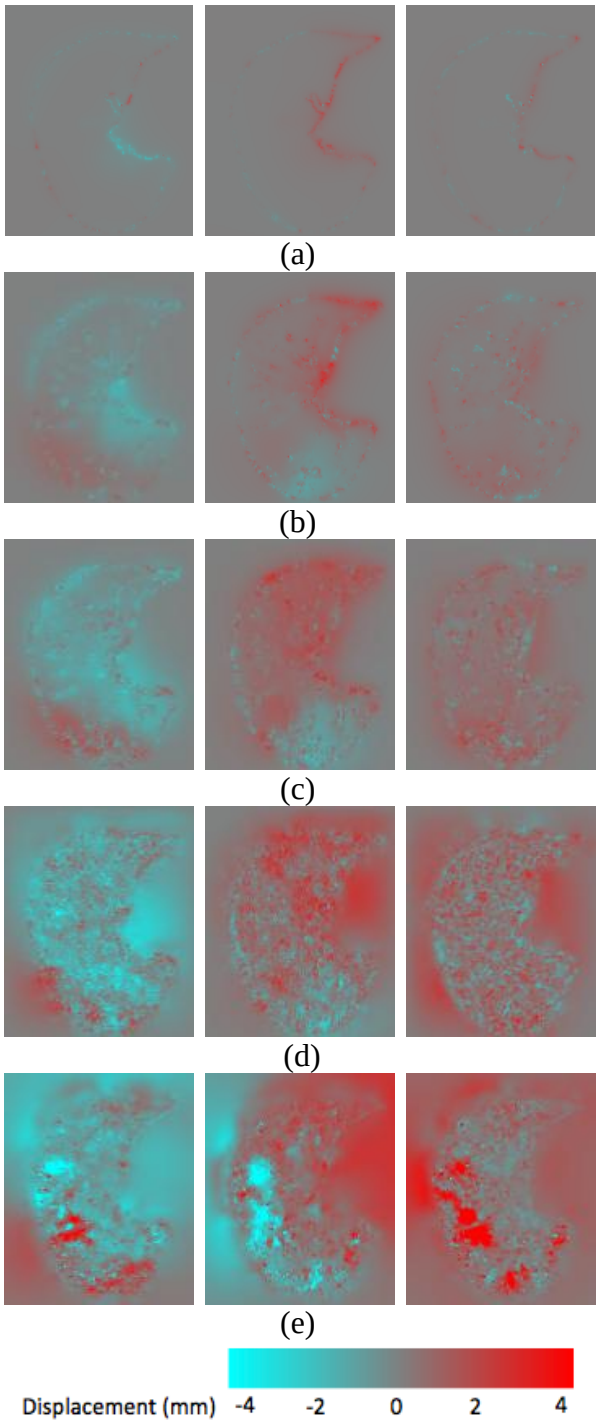

Figure 10: MLMR method registration from first anatomy level to the last anatomy level, and comparison with multi-resolution method. (a) lung surface only; (b) surface and large blood vessel; (c) lung surface, large and small blood vessels; (d) Final result by MLMR; (e) Final result by multi-resolution method. Columns from left to right are displacement along x-axis, y-axis and z-axis.

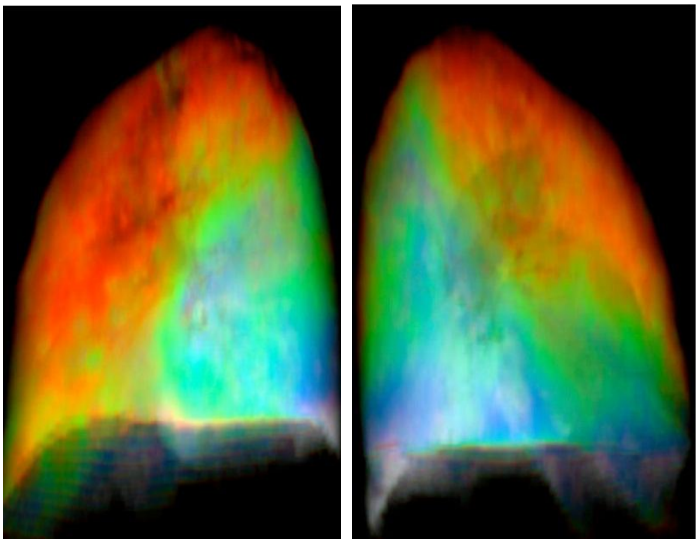

(a)

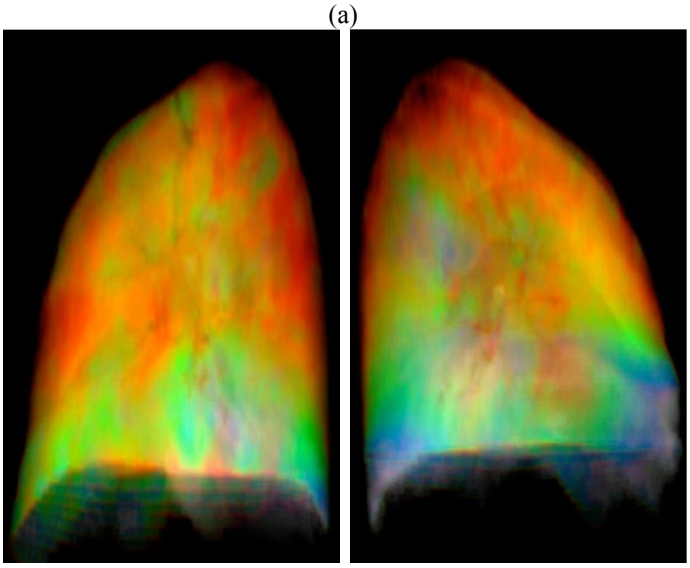

(b)

Figure 11: The 3D lung displacement magnitude computed by MLMR registration.

Figure 11 represents the 3D volume rendered distribution of the volumetric lung displacement magnitude obtained from two different 4D-CTs of the same patient. The range of values are color-coded as: 0 voxel – black, 1 voxel – red, 2 voxels – yellow, 3 voxels – green, 4

voxels – blue, and 5 voxels – white. Such distribution shows the 3D heterogeneity in the motion of the lung. Additionally, it can be seen that the 4D-CT imaging taken for the same patient before a different treatment fraction shows a different volumetric lung displacement. Such variations in the breathing can be attributed to voluntary and involuntary breathing changes, which can be captured using spirometry and impulse oscillometry measurements. This further shows the need for generating subject specific lung models that will account for such everyday variations.

5.2 Validation of MLMR Registration Results

4D-CT patient datasets are registered for validation purpose. Multi-resolution optical flow registration method (Guerrero, et al., 2006) is used as one of the reference methods. Since our MLMR registration method is based on multi-resolution optical flow registration method but add multi-level component and TPS to address the intensity variation issue, comparing MLMR method with multi-resolution method especially shows the performance of our modified component of optical flow to address the intensity variation issue. Some of the state-of-art registration methods, including the demons method, free-form registration method, are used in addition to the multi-resolution optical flow for validating the 4D-CT registration method. The implementation of these registration algorithms is from the DIRART software suite (Yang, et al., 2010). The registration accuracy in this case is represented using TRE and the inverse consistency error. Additionally, the Jacobian value computed for the 4D-CT datasets using the proposed method as well as the different registration methods is discussed.

Table 2: TRE comparison of MLMR and Multi-Resolution method (unit: mm)

Inhalation	Segmentation	Methods	Subject1	Subject2	Subject3
0%-30%	Intensity thresholds	MLMR 3 levels TPS	1.79 ±0.92	1.92 ±1.02	1.69 ±0.90
		MLMR 4 levels TPS	1.52 ±1.01	1.82 ±1.41	1.49 ±0.89
		MLMR 4 levels no TPS	1.67 ±0.84	2.26 ±1.41	1.64 ±0.91
		Multi-Resolution	1.72 ±0.89	1.95 ±1.33	1.39 ±0.81
	Seed-growing Single Level	MLMR 3 levels TPS	2.04 ±1.05	2.09 ±1.17	1.69 ±0.78
		MLMR 4 levels TPS	1.81 ±1.05	1.94 ±1.28	1.47 ±0.90
		MLMR 4 levels no TPS	1.75 ±1.08	2.28 ±1.29	1.64 ±1.06
		Multi-Resolution	1.72 ±0.89	1.95 ±1.33	1.39 ±0.81
	Seed-growing Double Levels	MLMR 3 levels TPS	1.98 ±1.31	2.15 ±1.09	1.78 ±0.75
		MLMR 4 levels TPS	1.75 ±0.85	2.10 ±1.28	1.62 ±0.88
		MLMR 4 levels no TPS	1.85 ±0.83	2.72 ±1.71	1.84 ±0.80
		Multi-Resolution	1.72 ±0.89	1.95 ±1.33	1.39 ±0.81
0%-60%	Intensity thresholds	MLMR 3 levels TPS	1.89 ±1.01	1.96 ±1.26	1.96 ±1.08
		MLMR 4 levels TPS	1.76 ±1.14	2.10 ±1.23	2.13 ±1.41
		MLMR 4 levels no TPS	2.53 ±1.89	2.19 ±1.20	2.46 ±1.49
		Multi-Resolution	2.48 ±1.87	2.56 ±1.57	2.99 ±1.74
	Seed-growing Single Level	MLMR 3 levels TPS	2.49 ±1.68	2.58 ±1.29	2.81 ±1.49
		MLMR 4 levels TPS	1.98 ±1.33	2.19 ±1.26	2.41 ±1.52
		MLMR 4 levels no TPS	2.38 ±1.71	2.66 ±1.38	2.73 ±1.87
		Multi-Resolution	2.48 ±1.87	2.56 ±1.57	2.99 ±1.74
	Seed-growing Double Levels	MLMR 3 levels TPS	2.39 ±1.77	2.52 ±1.37	2.89 ±1.58
		MLMR 4 levels TPS	2.01 ±1.36	2.25 ±1.18	2.26 ±1.29
		MLMR 4 levels no TPS	2.31 ±1.58	2.39 ±1.34	2.81 ±1.73
		Multi-Resolution	2.48 ±1.87	2.56 ±1.57	2.99 ±1.74
0%-100%	Intensity thresholds	MLMR 3 levels TPS	2.24 ±1.38	2.33 ±1.19	2.00 ±1.00
		MLMR 4 levels TPS	2.31 ±1.57	2.92 ±1.49	2.51 ±1.32
		MLMR 4 levels no TPS	3.01 ±1.81	3.19 ±1.74	2.48 ±1.18
		Multi-Resolution	3.52 ±1.98	3.82 ±1.89	3.41 ±1.75
	Seed-growing Single Level	MLMR 3 levels TPS	3.10 ±2.05	3.40 ±1.66	3.77 ±1.64
		MLMR 4 levels TPS	2.53 ±1.64	3.73 ±1.76	3.32 ±1.74
		MLMR 4 levels no TPS	2.93 ±1.75	3.76 ±1.94	4.16 ±1.71
		Multi-Resolution	3.52 ±1.98	3.82 ±1.89	3.41 ±1.75
	Seed-growing Double Levels	MLMR 3 levels TPS	3.00 ±2.05	3.46 ±1.60	3.87 ±1.74
		MLMR 4 levels TPS	2.56 ±1.36	3.50 ±1.96	3.09 ±1.51
		MLMR 4 levels no TPS	2.80 ±1.64	4.11 ±2.16	4.07 ±1.68
		Multi-Resolution	3.52 ±1.98	3.82 ±1.89	3.41 ±1.75

Both the proposed method and multi-resolution optical flow registration method estimate motion on the whole volume of patient data. To evaluate the accuracy of the registration methods, landmarks were first manually picked by a clinician through all of the volumes. The landmarks' motion estimations using each of the registration methods were then compared. Ground truth motion on these landmarks are the landmark displacements from one volume to another marked by the clinician, while computed motion estimations of those landmarks are the displacement vectors computed using each of the 4D-CT registration method. Accuracy is presented in the form of Target Registration Error (TRE) and inverse consistency error values. TRE is a straightforward indicator to represent the difference between computed displacement and ground-truth displacement. Lower TRE values represent better registration results.

Table 2 shows the TRE estimation for five subjects when the landmarks are tracked between 0% inhalation to 30% inhalation volume, 0% - 60% inhalation volume, and 0% - 100% inhalation volume, respectively. Four different registration approaches with both intensity thresholds and seed-growing segmentation options are investigated. In the first case, three levels of anatomical representation are used along with the TPS. The three levels of anatomical representation for the three patients include the surface lung, surface lung together with the large vessels, and the combination of surface lung, large and small vessels. It can be seen that for the first patient the TRE has a mean of 2.24 mm with a standard deviation of 1.38 mm for the case of 0% inhalation volume registered with 100% inhalation volume. For the second patient, a mean TRE of 2.33 mm with a standard deviation of 1.19 mm was obtained. When the parenchymal region is considered as an additional anatomical level (for four total anatomical levels) and along with TPS, the TRE increases to a mean of 2.31 mm with a standard deviation of 1.57 mm for the

first patient and to a mean of 2.92 mm with a standard deviation of 1.49 mm. This is because of the low contrast in the intensity for the parenchymal region. When the registration is performed without the use of TPS, the mean TRE for the first patient is 3.01 mm with a standard deviation of 1.81 mm and the mean TRE for the second patient is 3.19 mm with a standard deviation of 1.74 mm. Thus for registering the parenchymal region, the thin plate splines showed an improved accuracy as compared to optical flow registration. When compared with the results obtained from multi-resolution optical flow the mean TRE for the first patient is 3.52 mm with a standard deviation of 1.98 mm and mean TRE for the second patient is 3.82 mm with a standard deviation of 1.89 mm. Similar results were observed for all the three patients supporting the observation that the proposed MLMR optical flow registration with three levels of anatomy provides a TRE less than 3 mm.

For the maximum displacement errors for the landmarks, Figure 12 plots of the TRE for ten landmarks of a 4D-CT, which are distributed as three for upper, three for middle and four for the lower region. The TRE is plotted for 0%-30% (Figure 12(a)), 0%-60% (Figure 12(b)) and 0%-100% (Figure 12(c)) of the inhalation volume. It can be seen that the maximum displacement error for the multi-resolution optical flow is approximately 19 mm (Figure 12(c)), while for the same landmark, using the 3 levels of anatomical representation in the proposed method yields a maximum displacement of 6 mm. It can be seen that the maximum displacement error for the proposed displacement is lower when compared to the multi-resolution optical flow approach.

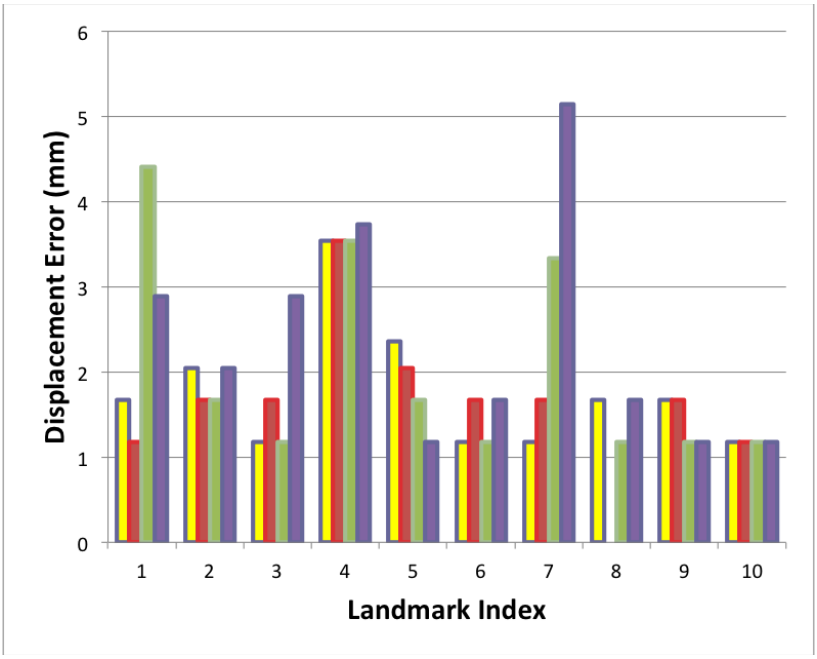

Figure 12(a)

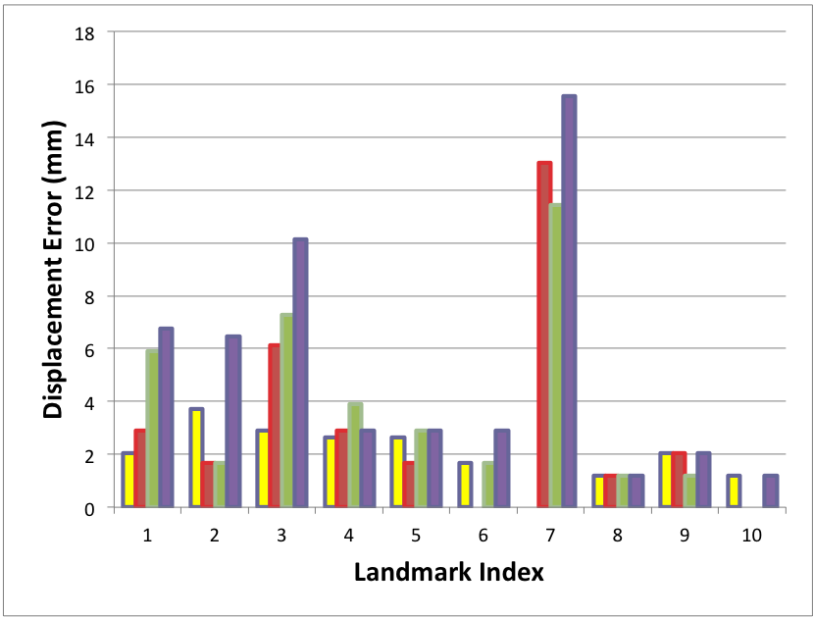

Figure 12(b)

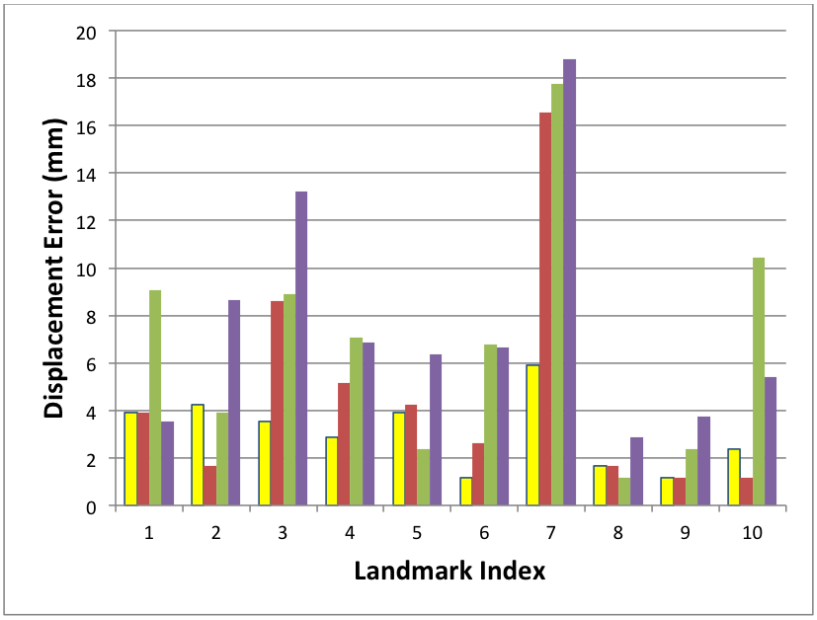

Figure 12(c)

Figure 12(d)

Figure 12: Error of computed displacement comparing with ground-truth displacement (by voxel distance) for landmarks of one patient data. (a), (b) and (c) show error for 0% to 30% ,0% to 60% and 0% to 100% inhalation process respectively; (d) legend.

The mean and standard deviation of the TRE is tabulated in Table 3 for each of methods considering all the lung volumes of each of the 4D-CT datasets. When look into TRE of subject 5, it can be seen that the MLMR optical flow with 3 levels of anatomy provides a mean TRE of 2.25 mm. When compared with Multi-Resolution optical flow method with the TRE of 6.93 mm and non-optical flow methods (demons, free form and inverse consistent demons) with the TRE of 10.37, 16.90 and 8.11 mm, respectively, the proposed method yields an accurate 4D-CT registration results. Such variations in the result can be attributed to the landmark intensity inconsistency issue inherent in the 4D-CT datasets.

Table 3: TRE comparison of registration methods for 4D-CT datasets (unit: mm)

Method	Subject 1		Subject 2		Subject 3		Subject 4		Subject 5	
	Mean	STD	Mean	STD	Mean	STD	Mean	STD	Mean	STD
MLMR optical flow 3 levels TPS	2.28	1.25	2.25	1.56	2.93	2.78	1.79	1.44	2.25	2.21
MLMR optical flow 4 levels TPS	3.15	3.68	2.94	2.05	4.51	3.72	2.50	2.31	3.82	3.02
MLMR optical flow 4 levels no TPS	4.25	4.05	3.61	2.37	4.93	3.99	3.80	2.99	5.92	3.52
Multi-Resolution optical flow	5.06	4.43	4.35	3.50	5.40	4.34	4.68	3.60	6.93	3.81
Demons method	30.27	2.49	11.82	5.12	19.93	6.88	7.10	5.10	10.37	4.98
Free Form Deformation method	22.96	5.68	10.89	4.44	16.50	5.35	11.28	5.00	16.90	6.87
Inverse Consistent Demons method	11.19	3.98	5.13	2.60	7.41	4.93	5.13	4.46	8.11	4.35

The mean of the Jacobian is computed using DIRART software suite (Yang, et al., 2010) and is tabulated in Table 4 for each of the methods. The Jacobian determinant value is positive and increases as the lung volume increases for each of the methods. However, the inconsistent intensity value introduced errors in the non-optical flow methods' displacement estimation that caused inconsistency in the correlations of the Jacobian value. The Multi-Resolution optical flow method yielded a better consistency in the linear correlations of the Jacobian value because of its smoothening component. The proposed method yielded results that showed a more consistent linear increase in the Jacobian value.

Table 5 shows the inverse consistency results for the five 4D-CT datasets. A three level anatomy with TPS for parenchyma registration was used for this analysis. The consistency error for each patient is calculated by comparing the source 3D-CT displacement results obtained by registering the target with the source 3D-CT displacement results obtained by registering the source with the target. It can be seen that the proposed method has a consistency error in the range of 1 to 3 mm distance, which is better than as previously reported by (Murphy, van Ginneken, Pluim, Klein, & Staring, 2008).

Table 4: Mean of the Jacobian comparison for the registration methods (unit: mm)

			MLMR 3 levels TPS	MLMR 4 levels TPS	MLMR 4 levels no TPS	Multi-Resolution optical flow	Demons	Free Form Deformation	Inverse Consistent Demons
Subject 1	Left lung	0%-30%	1.0232	1.0282	1.0289	1.034	1.0494	1.01	0.9714
		0%-60%	1.142	1.1409	1.1394	1.1412	1.0038	1.0259	0.9596
		0%-100%	1.1898	1.1907	1.1961	1.2297	1.1044	1.0168	0.9665
	Right lung	0%-30%	1.0312	1.0391	1.039	1.0458	0.9216	0.8965	0.958
		0%-60%	1.1277	1.1397	1.1449	1.2144	0.96	0.95	0.9256
		0%-100%	1.1715	1.2092	1.2455	1.2921	0.97	0.98	0.9505
Subject 2	Left lung	0%-30%	0.97	0.9569	0.9529	0.9658	1.0435	1.0927	1.036
		0%-60%	1.044	1.0525	1.0512	1.12	0.9542	0.9972	0.9987
		0%-100%	1.0598	1.0872	1.0842	1.6526	1.0616	0.997	1.0165
	Right lung	0%-30%	0.9722	0.9724	0.9734	0.9571	0.9806	1.008	1.0348
		0%-60%	1.0391	1.0673	1.0661	1.065	0.8917	0.9092	0.9802
		0%-100%	1.0477	1.0788	1.0782	1.064	0.9242	0.94	0.9733
Subject 3	Left lung	0%-30%	1.009	1.0211	1.02	1.0236	1.0471	0.9557	0.9724
		0%-60%	1.0693	1.131	1.1302	1.1153	0.9488	0.9613	0.9214
		0%-100%	1.0967	1.183	1.1906	1.2932	0.8926	0.9646	0.9307
	Right lung	0%-30%	1.0199	1.0224	1.0187	1.0268	0.9744	0.98	0.9798
		0%-60%	1.0759	1.1319	1.1328	1.1328	0.8861	0.8929	0.9304
		0%-100%	1.1054	1.1693	1.1698	1.5978	0.8473	0.9078	0.9159
Subject 4	Left lung	0%-30%	1.012	1.0532	1.05	1.0623	1.0771	1.043	1.0653
		0%-60%	1.093	1.163	1.1633	1.1853	1.0923	1.082	1.0993
		0%-100%	1.117	1.209	1.2226	1.3232	1.112	1.134	1.122
	Right lung	0%-30%	1.023	1.0532	1.0212	1.0668	0.9764	1.002	1.043
		0%-60%	1.0799	1.1673	1.1658	1.1248	1.021	1.075	1.0802
		0%-100%	1.1402	1.1924	1.1933	1.6278	1.054	1.143	1.129
Subject 5	Left lung	0%-30%	1.01	1.0421	1.04	1.05	1.042	1.037	1.074
		0%-60%	1.081	1.147	1.143	1.1673	1.073	1.094	1.135
		0%-100%	1.102	1.189	1.2114	1.3193	1.105	1.145	1.167
	Right lung	0%-30%	1.011	1.0416	1.017	1.0475	1.05	1.002	1.067
		0%-60%	1.0659	1.1527	1.1523	1.1195	1.08	1.114	1.096
		0%-100%	1.1202	1.1811	1.1873	1.3245	1.113	1.178	1.125

Table 5: Consistency error for the MLMR method with three levels of anatomy and TPS based propagation, intensity thresholds segmentation. (unit: mm)

Inhalation	Subject 1		Subject 2		Subject 3		Subject 4		Subject 5	
	Left lung	Right lung	Left lung	Right lung	Left lung	Right lung	Left lung	Right lung	Left lung	Right lung
0%-30%	1.43	1.23	1.11	1.08	0.73	1.18	1.12	0.97	1.67	1.04
0%-60%	2.89	2.73	1.51	1.15	2.35	1.9	1.48	1.02	1.83	1.19
0%-100%	3.58	3.3	2.37	1.74	3.1	2.2	2.24	1.37	2.02	1.67
Average	2.63	2.42	1.66	1.32	2.06	1.76	1.61	1.12	1.84	1.30

5.3 Summary

In summary, the usage of MLMR optical flow with three levels of anatomy and TPS to propagate the results, from one anatomical level to another, yielded a minimal TRE for each of the five 4D-CT volume datasets, as well as the overall dataset. Additionally, the maximum landmark error was also shown to be minimal as compared to both Multi-Resolution optical flow method as well as non-optical flow methods. The inverse consistency of the displacements was also shown to be less than 2 mm. Finally, the Jacobian value associated with each of the computed volumetric displacement also increases linearly with an increase in the volume. Such result shows that the proposed method facilitates a 4D-CT registration with higher accuracy.

CHAPTER 6: DOSE CALCULATION AND SIMULATION USING 4D-CT LUNG REGISTRATION

One of the main problems in lung radiation therapy is to simulate and visualize the effect of intra-fraction breathing changes on the radiation dose delivered to the tumor. Such a simulation and visualization may lead to real-time adaptive radiation therapy, which enables doctors to change the patient's treatment during the radiation therapy.

Lung deforms during breathing according to the patient's body orientation and physiological condition, thereby changing the tumor location. This complex tumor motion subsequently compromises the accurate deposition of radiation dose on the tumor, and also increases the dose deposition on the surrounding lung tissues. Simulation and modeling of the 3D lung dosimetry forms an effective tool for calculating the amount of dose delivered on a moving lung tumor during radiotherapy (Santhanam A. , Willoughby, Meeks, Rolland, & Kupelian, 2009). Efforts have also been made to model the subject-specific 3D lung tumor motion by first developing the 3D lung surface dynamic model and then coupling it with the lung tumor using elastostatic springs (Santhanam A. , Willoughby, Meeks, Rolland, & Kupelian, 2008). Such methods demonstrate an approach to calculate the amount of dose delivered on the lung tumor during treatment. However, a key knowledge gap that needs to be addressed is the amount of radiation dose delivered to the surrounding lung tissues. Additionally, the deforming nature of the lung tumor was not used for calculating the amount of the dose delivered on the tumor.

From a simulation perspective, the simulation and visualization of subject-specific 3D lung conformal dosimetry is enabled by the usage of the following three clinical aspects: (i) usage of patient-specific anatomy, (ii) usage of patient-specific dose delivery and (iii) usage of the patient-specific tumor motion. The usage of patient-specific 3D volumetric lung anatomy allows the simulation to more accurately model the patient's tumor shape as well as account for the doses to normal structures as defined by the contours in the initial CT scan. This model could be extended to include target areas inside the lung where real-time dose calculations may be of benefit.

The usage of dynamic dose fields for computing the tumor dose accumulation accounts for the lung tumor motion as the normal lung tissue is displaced by the tumor. This is made possible by using a dose model approach for calculations that, in addition to determining the location of a voxel relative to the dose space, also include the electron density of that voxel and the appropriate dose related to that density.

The usage of advanced technologies within radiation oncology is able to give more specific patient motion information throughout the course of treatment. Some of these technologies allow the real-time tracking of the tumor motion by means of radiofrequency (RF) signaling devices that can be implanted into the tumor and tracked in real time during radiotherapy (e.g. Calypso System™ (Calypso Medical, Seattle, WA)) (Langen, et al., 2008). Acquiring additional information regarding the patient motion involves using 4D-CT scans to determine the extent of various organ deformations during the course of breathing. A long-term goal of this work is to account for the respiratory, cardiac or digestive motion by modeling the relationships of various anatomical structures involved in these motions as deformable objects in

the simulation framework.

A key issue faced by the simulation framework is the real-time requirement for clinical applicability. The real-time simulations of the actual location and shape of the tumor during the delivery of radiation enable the better understanding of the anatomy and the overall effects of each gantry angle and how each relates to the deforming target motion. Better understanding of these motions coupled with delivery techniques could lead to improved conformal radiation delivery. An average breathing rate for a human subject is approximately 5 seconds (West, 1995). Lung tumors are known to move approximately 1–3 cm during breathing (Shirato, Seppenwoolde, Kitamura, Onimura, & Shimizu, 2004). The simulation framework is required to compute the dose accumulated on the deforming 3D lung volume with the same spatio-temporal requirements while maintaining the maximum number of tumor motion steps.

In this chapter, a GPU-based dose calculation and simulation framework (Min, Santhanam, Neelakkantan, Ruddy, Meeks, & Kupelian, 2010) is presented. It allows dose to be calculated for dynamic anatomy and visualized in real time. The key contribution is to account for the patient-specific lung anatomy; dynamic lung motion and treatment planning together address the specific knowledge-gap associated with the radiation dose delivery for moving lung tumors. The key method proposed in this chapter is a method to compute the dose for the deforming lung anatomy using well-known and validated 3D dose convolutions on a modern state-of-the-art GPU. 2D Dose fluencies based on pre-calculated doses from a treatment plan are used as an input to compute the 3D dose accumulation on a moving lung tumor. These dose calculations are visualized in conjunction with the visualization of the 3D deforming lung anatomy in real time while the radiation is delivered. A method to account for the patient-

specific breathing during the treatment using optical flow based volumetric lung deformation is also discussed. This simulation method also facilitates the real-time computation of dose accumulation visualizing the effects from each individual beam. Additionally, the usage of optical-flow-based estimation of the 3D volumetric lung deformation facilitates a higher number of discrete phases as compared to the 4D-CT.

The simulation framework uses a 3D spherical volumetric manifold as a tumor, simulates a user-defined lung tumor motion and computes and displays in real time the dose accumulation on the tumor.

6.1 3D Dose Convolutions

A detailed discussion on the 3D dose convolution technique is provided by (Shirato, Seppenwoolde, Kitamura, Onimura, & Shimizu, 2004), (Mackie, Scrimger, & Battista, A convolution method of calculating dose for 15-MV x rays, 1985), (Mackie, Bielajew, Rogers, & Battista, 1988), (Papanikolaou, Mackie, Meger-Wells, Gehring, & Reckwerdt, 1993), (Boyer & Mok, 1985), (Boyer, Zhu, Wang, & Francois, 1989). For clarity, a brief description of the formulation is included. Convolution dosimetry first models the fluence of incident energy from the linear accelerator before interacting in the patient. Kernels, pre-calculated using the Monte Carlo method, then model the charged particle transport and photon scattering in the patient. For an inhomogeneous phantom, the dose D, at any point can be obtained by the superposition form

$$D(\vec{r}) = \int_V \frac{\mu}{\rho}(\vec{r} - \overrightarrow{r'}) \cdot \Psi(\vec{r} - \overrightarrow{r'}) \cdot K(\rho \cdot l\left(\overrightarrow{r'}\right), \vec{\omega}) d^3\overrightarrow{r'}$$

where $\frac{\mu}{\rho}$ is the mass attenuation coefficient, Ψ is the primary photon energy fluence, K is the

Monte Carlo-generated kernel, $\rho \cdot l\left(\overrightarrow{r'}\right)$ is the radiological path length, $\vec{r}$ is the distance from the source to the dose deposition site, $\overrightarrow{r'}$ is the distance from the source to the primary interaction site and $\vec{\omega}$ is the direction from the primary interaction site to the dose site (Papanikolaou, Mackie, Meger-Wells, Gehring, & Reckwerdt, 1993). It is to be noted that (Boyer, Zhu, Wang, & Francois, 1989) further expanded the above formulation by dealing with the delivered dose and energy in three steps. In the first step, the primary beam fluence and energy are computed as a convolution function. A GPU-based implementation of computing the primary beam fluence is also discussed in (Hopf & Ertl, 1999) using GPU based ray projection techniques (Engel, Hadwiger, Kriss, Salama, & Weizkopf, 2006) applied to Siddon's algorithm (Siddon, 1985). The primary beam fluence is then convolved with the CT image for computing the dose distributed because of the first scattering and multiple scattering. In this paper, we employ the formalization detailed by Boyer et al for calculating the dose and energy delivered to a CT volume.

All calculations in this work were performed for a 6 MV from a 21IX linear accelerator (Varian Medical Systems, Palo Alto, CA). The spectrum for the polyenergetic beam was obtained from the clinically commissioned beam used in the Pinnacle (Philips Medical Systems, Andover, MA) planning system at MD Anderson Cancer Center Orlando.

The convolution/superposition method, faster than Monte Carlo simulation, is still relatively time consuming. Benchmarks in the literature show that the CPU-based convolution calculations require approximately a few minutes to compute the dose per beam ((Santhanam A. , Willoughby, Meeks, Rolland, & Kupelian, 2009), (Hissoiny, Ozell, & Despres, 2009)). Advances in computer hardware have increased the speed of these computations, but convolution

calculations using commercially available systems still require on the order of 0.25–0.5 min per beam.

6.2 GPU-Based Separable 3D Dose Convolution

The 3D dose convolution is performed using a 3D separable dose convolution approach discussed by (Hopf & Ertl, 1999). A schematic flowchart representing the separable dose convolution is shown in Figure 13. In this method, a 3D dose convolution is split into row-wise, column-wise and plane-wise 1D convolutions. The 10 cm^3 sized lung data have been taken from a CT dataset with 128 slices and the 3D data with 1283 voxels are created. The 1D convolutions are computed for each voxel using its 127 neighbors along the row, column and plane, respectively. For real-time purposes, we employed a shared-memory-based data access for performing the convolutions. Specifically, the 3D CT data representing the patient anatomy, the displacement vector associated with each voxel and the voxels representing the 3D dose accumulated on each image voxel are copied into the shared memory of the GPU. The row and column 1D convolutions for each voxel initiate bulk data transfer between the GPU processor and the shared memory thereby increasing the memory bandwidth usage. However, the hardware architecture of the GPU does not directly allow for initiating bulk data transfer from the processor. Thus in the proposed method, we introduce an optimization where a 3D matrix transpose is performed after the row and column 1D convolution. Such a matrix transpose re-arranges the voxels from neighboring planes to be placed next each other thereby facilitating bulk data transfer.

An initial flux of 6 MV photons is assumed and a 3D dose is computed for each lung voxel as discussed in section 6.1. To calculate first scattering dose components, the 3D dose is

convolved with a kernel of size 33. The kernel is computed using the image voxels surrounding each point to be convolved as explained in section 6.1.

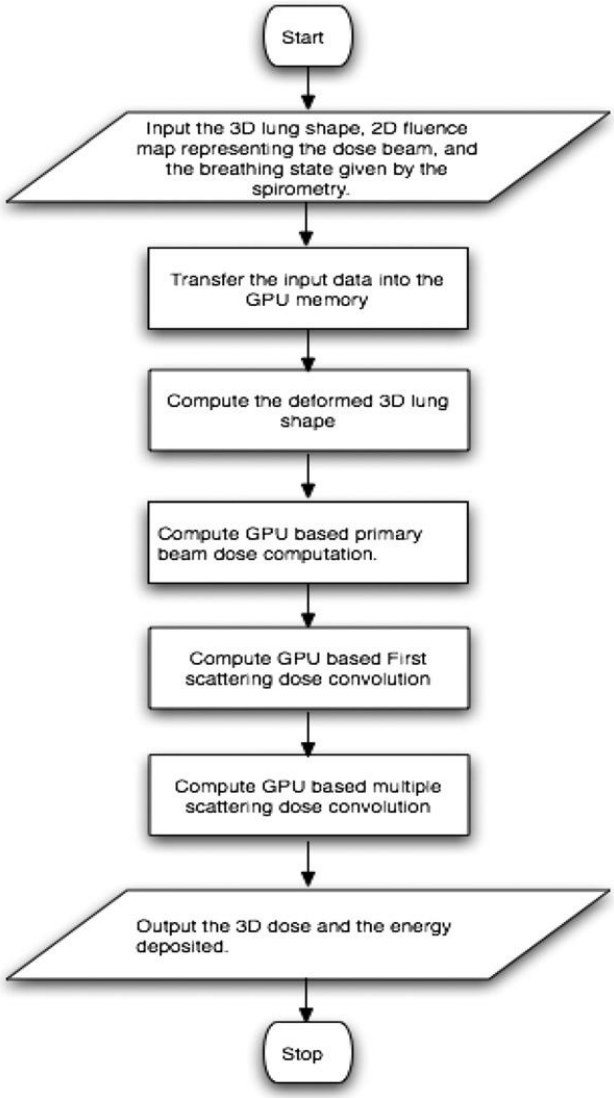

Figure 13: A schematic representation of the steps taken in the dose calculation of a moving tumor

6.3 MLMR Optical Flow Lung Registration

Lung volumes are registered with each other by MLMR optical flow registration method. In brief, each volume of the lung is segmented into 4 or 5 anatomical levels. In multi-resolution

optical flow registration iterations, displacements are calculated by weighted sum of displacements from nearby points in the volume. For the weighted sum calculation, different weights are given according to the anatomical level the point belongs to. Detail of MLMR registration method is discussed in Chapter 3 and 4.

6.4 Volume Visualization

A 3D GPU-based volume visualization is employed for visualizing the 3D lung volume together with the 3D lung dose accumulated on it. The method is implemented as follows. The 3D data representing the lung volume as well as the 3D dose accumulating on the lung volume are loaded into the processor as 3D textures. Once loaded, the 3D textures are volume projected into a 2D texture using CUDA-based perspective projection (Engel, Hadwiger, Kriss, Salama, & Weizkopf, 2006). The intensity of each voxel is used to determine the opaqueness of each voxel. For instance, the blood vessels inside the lung have a higher opaqueness as compared to the parenchyma region. Similarly, for the 3D dose, the region with a higher dose is considered to be more opaque. The GPU-based volume rendering first rotates the textures for the given viewing angle and then initiates rays from an origin in the direction given by the coordinate location of each voxel. As the ray is made to intersect with other voxels in the same direction the cumulative intensity value is then computed and associated with a 2D map. The final intensity of the 2D map represents the volumetric project of the 3D textures. Once both the 3D dose and the anatomy textures are projected onto to the 2D textures, they are then added and rendered. For clarity purposes, the 2D texture representing the 3D lung volume is rendered in RGB color while the 2D texture representing the 3D dose is rendered in gray-scale.

6.5 Implementation System

The implementation steps of the proposed framework are now described. A4D-CTlung volume was taken as a target for presenting the simulation framework. The 3DCT at the end-expiration lung volume was considered for planning the radiation treatment and the fluence maps and its associated azimuthal angles were generated and exported. As a general clinical protocol, a treatment plan with 5–7 beams was generated. The 4D-CTlung volumes are then segmented and registered with the end-expiration lung volume for computing the volumetric lung displacement during breathing. Before treatment, the spirometry equipment is assembled for the patient.

Figure 14(a) and Figure 14(b) show the spirometry mouth-piece administered for a volunteer. The volume-time breathing signal is subsequently collected and is given as input to the simulation framework. Figure 14(c) show a sample-breathing curve obtained for two subjects. During the treatment, the treatment time for each beam is noted and input to the simulation framework. The simulation framework simulates the volumetric lung displacement given by the lung volume from the spirometry signal coupled with the optical-flow-based registration. At each step of the displacement, the dose calculation using the proposed steps was performed and the energy delivered to each lung voxel is computed.

The implementation of the simulation framework was done in an Intel 8-core 2.6 GHz Mac Pro desktop. The source code for the computation and visualization was developed using C and NVIDIA CUDA. Two different graphic cards NVIDIA 8800 GT and NVIDIA GTX 285 were tested for performance analysis.

(a)

(b)

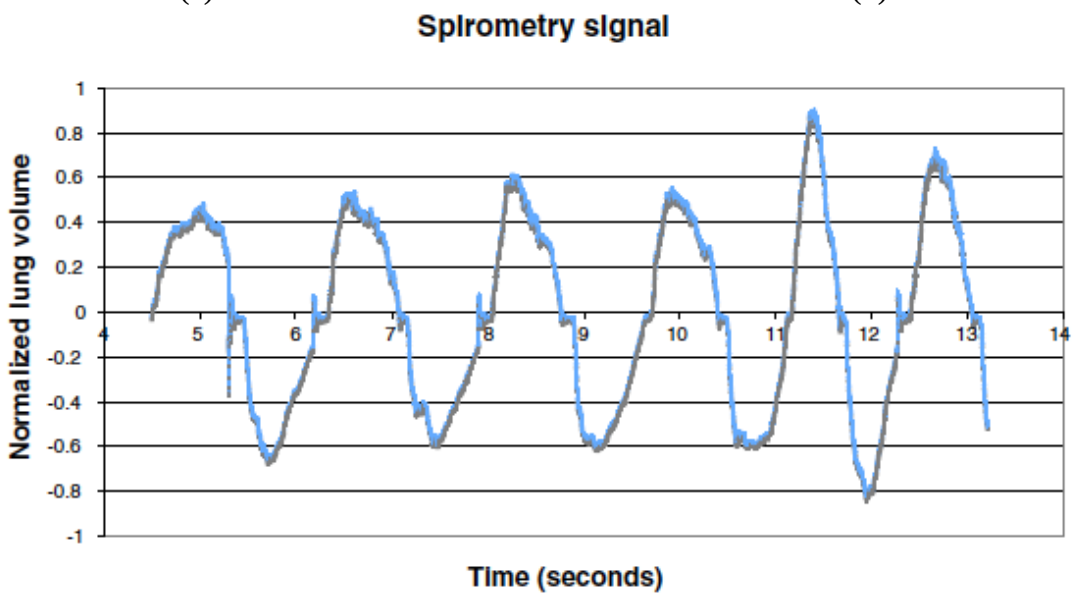

(c)

Figure 14: The facemask designed to hold the spirometry mouthpiece and the filter. (a) and (b) the usage of the facemask and the mouthpiece during imaging. (c) a normalized spirometry curve collected from a subject.

6.6 Simulation Results

Figure 15(a)–(c) represent the results of the simulation framework of dose delivered using a five-field conformal radiation dose distribution on a 3D matrix representing uniform tissue. In these images, the dose accumulated was normalized and illustrated as gray-scale values

normalized between 85 and 100% of the prescribed dose. The primary beam (Figure 15(a)), the first scattering (Figure 15(b)) and the multiple scattering (Figure 15(c)) are shown. The final dose delivered is the summation of the primary beam together with the first and the multiple scattering.

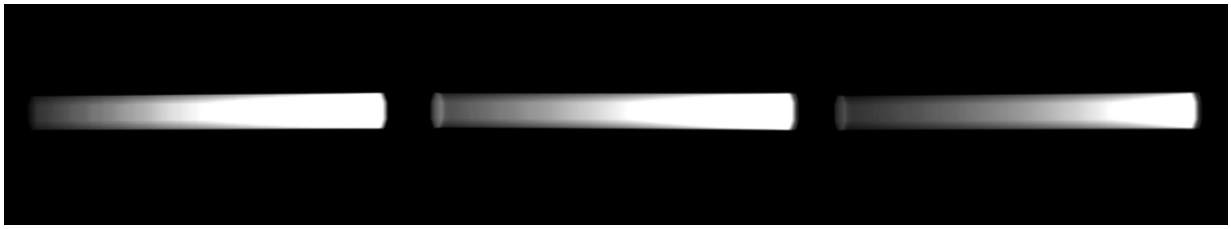

(a) (b) (c)

Figure 15: The dose beam for a 3D matrix representing uniform tissue with (a) the primary dose beam (b) the first scattering and (c) the multiple scattering.

Figure 16(a)–(c) represent the results of the simulation framework of dose delivered using a five-field conformal radiation dose distribution on a 3D lung CT dataset. The planned target volume margin for the tumor with a clinical tumor volume of 14.3 cm^3 is set to be 5 mm. The maximum motion of the tumor centroid was observed to be 7 mm. In these images, the dose accumulated was normalized and illustrated as gray-scale values normalized between 85 and 100% of the prescribed dose. The primary beam (Figure 16(a)), the first scattering (Figure 16(b)) and the multiple scattering (Figure 16(c)) are shown. It can be seen that there is no scattering outside the lung. Inside the lung, the scattering depends on the local anatomy and the air content, both of which are based on the HU value.

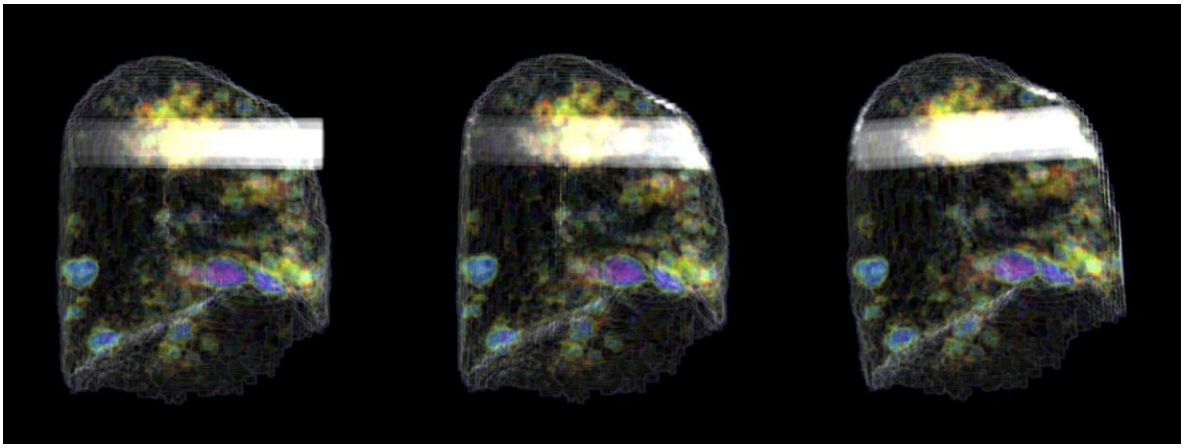

(a) (b) (c)

Figure 16: The dose beam for a 3D matrix representing 3D lung anatomy with (a) the primary dose beam, (b) the first scattering, and (c) the multiple scattering.

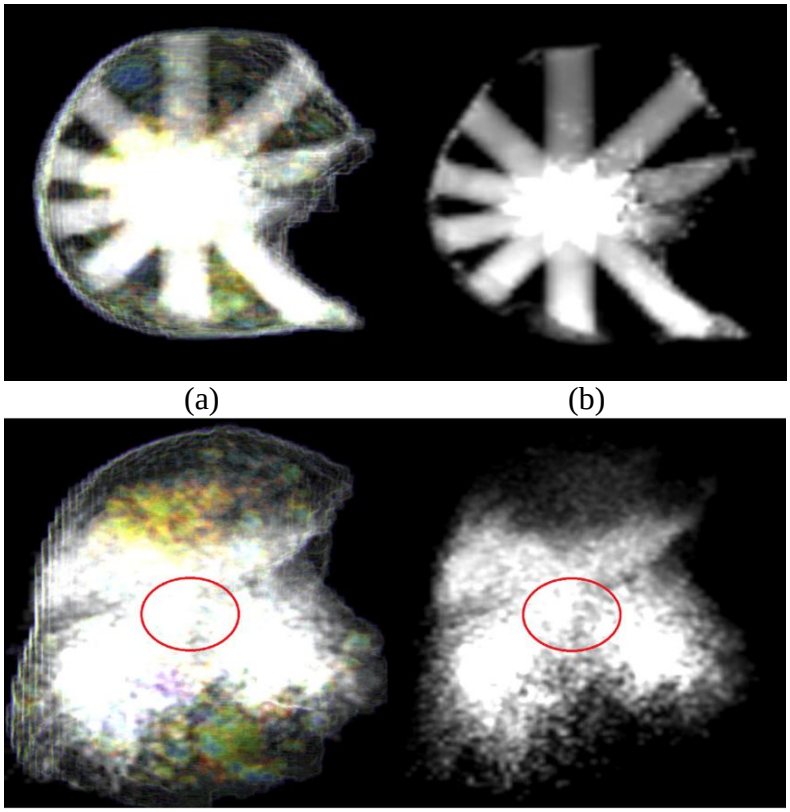

(a) (b)

(c) (d)

Figure 17: The 3D dose accumulated on the lungs with 3D static lung anatomy ((a) and (b)) and with 3D dynamic lung anatomy ((c) and (d)). Red circles indicate tumor areas: (a), (c) the 3D dose and the anatomy; (b), (d) the 3D dose only.

Figure 17(a) represents the dose delivered when no lung motion is considered as a

comparison to the planned treatment. Figure 17(a)–(d) show the 3D volumetric representations of the deforming 3D lung model and the dose accumulation considering the cases when the motion is considered and not considered. It can be seen that the tumor is well irradiated when it is not moving but a significant portion of it is under-dosed when motion is introduced. Additionally, it can be seen that the radiation dose is blurred throughout the entire treatment area and especially for the target when motion is introduced. These images illustrate the ability of the simulation framework to accumulate the dose from the treatment planning system while taking the lung motion into account. Additionally, from the simulation framework, the treatment efficacy can be estimated based on the amount of the radiation dose deposited on the surrounding lung tissues. Figure 17(b) represents the dose that was deposited to the 3D lung volume without the introduction of motion. It can be seen that the amount of dose (depicted by the white region) on the tumor is very high. Figure 17(d) represents the dose (depicted by the white region) that was accumulated in the lung tumor as the 3D lung volume was deformed using the subject-specific breathing conditions. The tumor region is marked using a red sphere in the two images. It can be seen that the amount of dose inside the tumor decreases with an increase in motion. Additionally, the motion of the surrounding tissues exposes them to the treatment dose. The motion of the surrounding tissues depends on the local tissue's motion as well as the patient's breathing. As illustrated in Figure 14, the motion of the lung varies from one breathing cycle to another and even from one patient to another. The proposed framework takes into account such variations and computes the delivered dose.

The simulation framework was programmed to represent different breathing conditions that may be observed in lung tumor patients. Figure 18(a) and Figure 18(b) show the dose

accumulation of a lung tumor and its surrounding tissues under two different breathing patterns acquired from a patient during radiotherapy. Figure 18(a) shows dose accumulation during a rapid shallow breathing pattern with a shortened expiration time. Figure 18(b) shows the dose accumulation in this patient with occasional deep inhalation and exhalation. In each of these cases, the amount of dose delivered to the tumor and surrounding tissues varies from one breathing pattern to another. The difference in the dose accumulation provides insight on the importance of considering breathing variations during radiation delivery. The gray-scale region represents the dose range between 85 and 100% of the prescribed dose on the isodose volume.

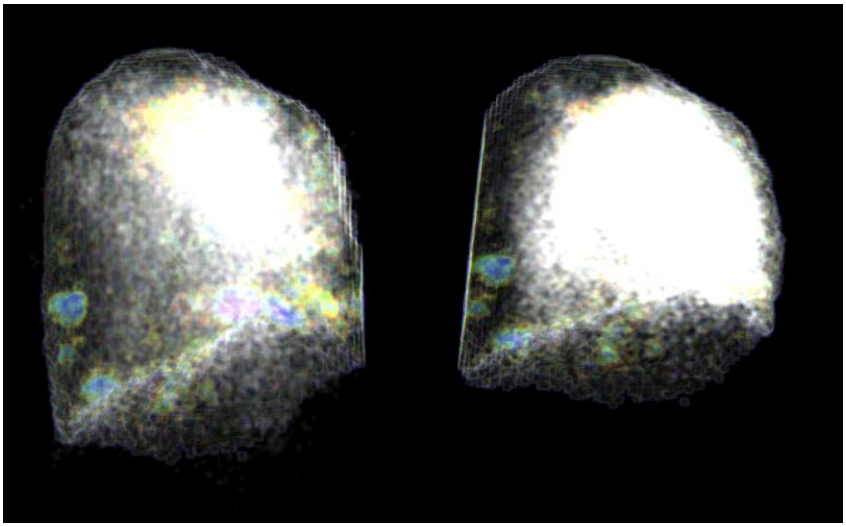

(a) (b)

Figure 18: 3D dose collection of a breathing lung during two different radiotherapy deliveries. The breathing in (a) was shallow and in (b) was occasional deep inhalation and exhalation.

6.7 Real-time Computation Issues

The real-time computation requirements are given by the fact that the step displacement of the tumor motion must not be more than 1 mm, which ensures the effectiveness of the search algorithm. Table 6 shows the run-time results of the simulation framework in relation to the 3

graphics cards utilized, all the tests ran with 128 mm^3 dose size, 128 mm^3 image size and 32 mm^3 kernel size. Two different approaches for memory access have been investigated: (1) texture memory and (2) shared memory. In each of these cases, 20 discrete steps were taken to represent a single breath, which is higher than the number of snapshots used in 4D-CT. It can be seen that in the case of using GTX 285, the dose calculation can be achieved in 300 ms. The primary dose is calculated in approximately 15 ms, a minimum speed-up of approximately 30 times when compared to (Hopf & Ertl, 1999). Additionally, the calculation of this dose is independent of the organ being investigated.

Table 6: GPU computational speed-ups

Method		Texture	Shared	Optimized shared memory
Row convolution time (ms)	NVIDIA 8800 GT	283	108	108
	NVIDIA GTX 285	149	52	52
	NVIDIA 9600 GT	423	257	253
Column convolution time (ms)	NVIDIA 8800 GT	279	119	119
	NVIDIA GTX 285	145	55	55
	NVIDIA 9600 GT	423	255	255
Plane convolution time (ms)	NVIDIA 8800 GT	291	191	108
	NVIDIA GTX 285	152	104	52
	NVIDIA 9600 GT	430	320	254

6.8 Summary

The framework simulates and visualizes the subject-specific motion of the lung tumor and its surrounding tissues and its dosimetry, it enables computing the dose accumulation on an

actual moving 3D lung volume in real time using modern state-of-the-art GPUs. It allows oncologists to have the ability to visualize and appreciate radiation dose deposition in a moving lung tumor.

CHAPTER 7: CONCLUSION

A multiple anatomical level multiple volume resolution based optical flow method is presented in this dissertation for registering 3D lung CT volumes. Using the motion data, we expand to a GPU based real-time framework of radiation dose delivery computation and visualization. The proposed method enables the usage of physics based volumetric lung deformations during lung radiotherapy. According to the dose delivery simulation from the physics based volumetric lung deformation model, radiation therapy planning can be accurate and intuitive for clinic experts.

When compared with optical flow methods using multi-resolution scheme alone, the presented method is able to better account for non-constant intensity of landmarks and low contrast; when compared with other registration methods, the presented method outperforms for these aspects as well.

Changing the intensity of a portion of the lung to a constant value in one volume, then changing the intensity of corresponding portion of the lung in the other volume to the same constant value, this scheme addresses the issue of landmark intensity variation, so that all of the corresponding points have an identical intensity. Such segmentations are set according to normalized local maxima intensity gradient value, which is also represented as intensity value of edge map on the CT slices.

The multi-level nature of the proposed registration facilitates accounting for noise issue of the optical flow approach for 4D-CT lung registration. In 4D-CT image registration, in some

regions feature intensities are quite similar to each other or close to noise intensity. Displacement estimation in such regions is not accurate due to the difficulty in finding the matched features. However, features in lung contour and regions around blood vessels are quite easily distinguished as they have high intensity contrast. Displacement estimations are accurate in these regions. The multi-level nature of the optical flow based registration method we propose is to first group voxels into several levels based on the local anatomical representation. During displacement calculation, the displacements for only those nearby voxels from the same level or the level easiest to be tracked are computed.

It can be observed that the estimated lung displacement is heterogeneous from air volume to another. In other words, the amount of voxel displacement varies for a given voxel from one lung volume to another. Additionally, it can also be seen that the displacement itself varies from one patient to another. Such subject to subject variations in the lung displacement further emphasizes the need for subject-specific physics based deformation models.

The radiation dose is simulated to accumulate on the entire 3D lung volume. Treatment plan for these lung tumors has been generated using five to seven beams. The radiation dose plan is extracted from the planning system as individual beam fluences. The simulation framework uses the extracted dose fluences as 2D matrices and simulates the dose accumulation in the 3D deforming lung CT using the proposed 3D dose calculation. The tumor motion is simulated using the subject-specific lung motion estimated from 4D-CT at a rate of 3–5 seconds per breathing. The real-time nature of the simulation framework is shown with and without motion steps per breathing and can be further optimized by the choice of the 3D lung voxel resolution and the subject's breathing rate. Simulation results show that the amount of dose accumulated in the lung

tumor depends on the motion during the radiation treatment.

The MLMR registration method is based on the segmentation of the lung anatomy at different levels of representation. The accuracy of the proposed method is thus dependent upon the accuracy of the segmentation procedure. In the proposed work, we have employed intensity thresholds automatic segmentation and seed-based region growing semi-automatic segmentation of the lung anatomy. Future work will better shed light on the usage of more different segmentation methods and evaluate their effect on the accuracy of the registration procedure, on a subject-by-subject basis. In addition, future work will also focus on minimizing the changes in the voxel intensity of landmarks during image acquisition without exposing the patient to more radiation during imaging.

For the GPU based real-time framework, it may further validate dose delivery using 4D programmable phantom studies and incorporate patient-specific deformable models for predicting the tumor motion. From the applications of these motions, the ultimate goal is to utilize the framework to manage the patient's treatment in real time. Using such a simulation and visualization framework, the physician could make decisions to adapt the radiation delivery by calculating the potentials for under- or over-dosing. This adaptive radiation therapy would allow the user to not only see what dose is being delivered but also to control the radiation delivery during the treatment. Furthermore, the method can also be extended from conformal dosimetry to dose calculations using intensity-modulated radiotherapy (IMRT), where the radiation dose delivered to the patient from a single gantry angle varies according to the dynamic multi-leaf collimator (MLC). Such implementations will further stress the utility of the real-time nature of the 3D dose calculations.

LIST OF REFERENCES

Altekruse, S., Kosary, C., Krapcho, M., Neyman, N., Aminou, R., Waldron, W., et al. (2010). *SEER Cancer Statistics Review, 1975-2007.* Bethesda, MD: National Cancer Institute.

American Cancer Society. (2010). *Cancer Facts & Figures 2010.* Atlanta: American Cancer Society.

Anand, P., Kunnumakara, A. B., Sundaram, C., Harikumar, K. B., Tharakan, S. T., Lai, O. S., et al. (2008). Cancer is a Preventable Disease that Requires Major Lifestyle Changes. *Pharmaceutical Research , 25* (9), 2097-2116.

Betke, M., Hong, H., & Ko, J. (2001). Automatic 3D Registration of Lung Surfaces in Computed Tomography Scans. *Medical Image Computing and Computer-Assisted Intervention 2001* (pp. 725-733). Berlin-Heidelberg: Springer.

Betke, M., Hong, H., Thomas, D., Prince, C., & Ko, J. P. (2003). Landmark Detection in the Chest and Registration of Lung Surface with an Application to Nodule Registration. *Medical Image Analysis , 7*, 265-281.

Blackall, J., Ahmad, S., Miquel, M., Landau, D., & Hawkes, D. (2004). Modeling respiratory motion for optimization of lung cancer radiotherapy using fast MR imaging and intensitybased image reigstration. *Proceedings of the International Society for Magnetic Resonance in Medicine*, *11*, p. 2610.

Boyer, A. L., Zhu, Y. P., Wang, L., & Francois, P. (1989). Fast Fourier transform convolution calculations of x-ray isodose distributions in homogeneous media. *Medical Physics , 16*, 248-253.

Boyer, A., & Mok, E. (1985). Aphoton dose distributionmodel employing convolution calculations. *12*, 169-177.

Brenner, D. J., & Hall, E. J. (2007). Computed Tomography — An Increasing Source of Radiation Exposure. *The New England Journal of Medicine , 357* (22), 2277-2284.

Christensen, G., Song, J., Lu, W., El, N. I., & Low, D. (2007). Tracking lung tissue motion and expansion/compression with inverse consistent image registration and spirometry. *Medical Physics , 34* (6), 2155-2163.

Danilouchkine, M. G., Mastik, F., & van der Steen, A. F. (2009). A study of coronary artery rotational motion with dense scale-space optical flow in intravascular ultrasound. *Physics in Medicine and Biology , 54* (6).

Engel, K., Hadwiger, M., Kriss, J. M., Salama, C. R., & Weizkopf, D. (2006). *Real-Time Volume Graphics.* Wellesley, MA: A K Peters.

Fan, L., & Chen, C. (1999). 3D warping and registration from lung images. *Proceedings of SPIE, 3660*, pp. 459-470.

Farin, G. E. (Ed.). (1987). *Geometric modeling: Algorithms and new trends.* Society for Industrial & Applied.

Guerrero, T., Sanders, K., Castillo, E., Zhang, Y., Bidaut, L., Pan, T., et al. (2006). Dynamic ventilation imaging from four-dimensional computed tomography. *Physics in Medicine and Biology , 51* (4), 777-791.

Guerrero, T., Zhang, G., Huang, T.-C., & Lin, K.-P. (2004). Intrathoracic tumour motion estimation from CT imaging using the 3D optical flow method. *Physics in Medicine and Biology , 49*, 4147.

Hilsmann, A., Vik, T., Kaus, M., Franks, K., Bissonette, J., Purdie, T., et al. (2007). Deformable 4DCT Lung Registration with Vessel Bifurcations. *Proc. Int. Conf. of Computer Assisted Radiology and Surgery (CARS 2007).* Berlin.

Hissoiny, S., Ozell, B., & Despres, P. (2009). Convolution-superposition dose calculations using GPUs. *Medical Physics , 37*, 2807.

Hong, W. K., Bast, R. C., Hait, W., Kufe, D. W., Holland, J. F., Pollock, R. E., et al. (2010). *Holland Frei Cancer Medicine 8th Edition* (Vol. 8). PMPH-USA.

Hopf, M., & Ertl, T. (1999). Accelerating 3D convolution using graphics hardware. *IEEE Conference on Visualization, 1*, pp. 471-474.

Horn, B., & Schunck, B. (1981). Determining optical flow. *Artificial Intelligence* , 185-203.

Johnson, H. J., & Christensen, G. E. (2001). Landmark and intensity-based, consistent thinplate spline image registration. (pp. 329-343). London: Springer-Verlag.

Johnson, H., & Christensen, G. (2002). Consistent landmark and intensity based image registration. *IEEE Transactions on Medical Imaging , 21* (5), 450-461.

K., M., van Ginneken, B., Pluim, J., Klein, S., & Staring, M. (2008). Quantitative assessment of registration in thoracic CT. *First International Workshop on Pulmonary Image Processing.* New York.

Klinder, T., Lorenz, C., von Berg, J., Renisch, S., Blaffert, T., & Ostermann, J. (2008). 4DCT image-based lung motion field extraction and analysis. *Medical Imaging 2008: Image Processing , 6914*, 69141L-69141L-11.

Kochanek, K. D., Xu, J., Murphy, S. L., Minino, A. M., & Kung, H.-C. (2011). Death: Preliminary Data for 2009. *National Vital Statistics Report , 59* (4), 69.

Langen, K. M., Willoughby, T. R., Meeks, S. L., Santhanam, A., Cunningham, A., Levine, L., et al. (2008). Observations on real-time prostate glandmotion using electromagnetic tracking. *International Journal of Radiation Oncology*Biology*Physics , 71*, 1084-1090.

Lucas, B., & Kanade, T. (1981). An Iterative Image Registration Technique with an Application to Stereo Vision. *Proceedings of Imaging Understanding Workshop*, (pp. 121-130).

Mackie, T. R., Bielajew, A. F., Rogers, D., & Battista, J. J. (1988). Generation of photon energy deposition kernels using the EGS Monte Carlo code. *Physics in Medicine and Biology , 33*, 1-20.

Mackie, T. R., Scrimger, J. W., & Battista, J. J. (1985). A convolution method of calculating dose for 15-MV x rays. *Medical Physics , 12*, 188-196.

McClelland, J., Blackall, J., Tarte, S., Chandler, A., Hughes, S., Ahmad, S., et al. (2006). A continuous 4D motion model from multiple respiratory cycles for use in lung radiotherapy. *Medical Physics , 33* (9), 3348-3358.

Min, Y., Santhanam, A., Neelakkantan, H., Ruddy, B. H., Meeks, S. L., & Kupelian, P. A. (2010). A GPU based framework for modeling real-time 3D lung tumor conformal dosimetry with subject-specific lung tumor motion. *Physics in Medicine and Biology , 55*, 5137-5150.

Murphy, K., van Ginneken, B., Pluim, J., Klein, S., & Staring, M. (2008). Quantitative assessment of registration in thoracic CT. *The First International Workshop on Pulmonary Image Analysis: MICCAI Workshop.*

National Center for Health Statistics. (2011). *Health, United States, 2010: With Special Feature on Death and Dying.* Hyattsville, MD: National Center for Health Statistics.

Pan, Y., Kumar, D., Hoffman, E. A., Christensen, G. E., McLennan, G., Song, J. H., et al. (2005). Estimation of regional lung expansion via 3D image registration. *Medical Imaging: Physiology, Function, and Structure from Medical Images. , 5746*, 453-464.

Papanikolaou, N., Mackie, T. R., Meger-Wells, C., Gehring, M., & Reckwerdt, P. (1993). Investigation of the convolution method for polyenergetic spectra. *Medical Physics , 20*, 1327-1336.

Rangarajan, A., H., C., & Duncan, J. (1999). Rigid point feature registration using mutual information. *Medical Image Analysis , 3* (4), 425-440.

Rohlfing, T., Maurer, C. R., O'Dell, W. G., & Zhong, J. (2004). Modeling respiratory motion for optimization of lung cancer radiotherapy using fast MR imaging and intensity-based image reigstration. *Medical Physics , 31* (3), 427.

Santhanam, A., Min, Y., Rolland, J., ImieLinska, C., & Kupelian, P. (2011). Four Dimentional Computational Tomography Lung Registration Methods. In A. El-Baz, & J. Suri (Eds.), *Computer Aided Diagnosis of Lung Imaging.* CRC Press.

Santhanam, A., Willoughby, T. R., Meeks, S. L., Rolland, J. P., & Kupelian, P. A. (2008). Real-time simulation of 3D lung tumor dosimetry. *Medical Image Computing and Computer Aided Intervention*, (pp. 710-717).

Santhanam, A., Willoughby, T., Meeks, S., Rolland, J., & Kupelian, P. (2009). Modeling simulation and visualization of 3D lung conformal dosimetry. *Physics in Medicine and Biology , 54* (20), 6165-6180.

Shirato, H., Seppenwoolde, Y., Kitamura, K., Onimura, R., & Shimizu, S. (2004). Intrafractional tumor motion: lung and liver. *Seminars in Radiation Oncology , 14* (1), 10-18.

Siddon, R. (1985). Fast calculation of the exact radiological path for the three dimensional CT array. *Medical Physics , 53*, 1337-1349.

Tai, X.-C., Lie, K.-A., Chan, T., & Osher, S. (Eds.). (2005). *Image Processing Based on Partial Differential Equations.* Springer.

Vik, T., Kabus, S., von Berg, J., Ens, K., Dries, S., Klinder, T., et al. (2008). Validation and comparison methods for free-breathign 4D lung CT. *Medical Imaging 2008: Image Processing , 6914*, 69142P-69142P-10.

Vogelstein, B., & Kinzler, K. W. (1998). *The Genetic Basis of Human Cancer.* McGraw-Hill.

West, J. B. (1995). *Respiratory Physiology, the Essentials.* Philadelphia, PA: Lippincott Williams and Wilkins.

Woods, K., Fan, L., Chen, C. W., & Wang, Y. (1999). Physics-based 3D warping and registration from lung images. *SPIE proceedings series , 3660*, 459-470.

Yang, D., Brame, S., Naqa, I. E., Aditya, A., Wu, Y., Goddu, S. M., et al. (2010). Technical Note: DIRART – A software suite for deformable image registration and adaptive radiotherapy research. *Journal of Medical Physics , 38* (1), 67-77.

Yang, D., Li, H., Low, D. A., Deasy, J. O., & Naqa, I. E. (2008). A fast inverse consistent deformable image registration method based on symmetric optical flow computation. *Physics in Medicine and Biology , 53* (21).

Zhang, G., Huang, T., Guerrero, T., Lin, K., Stevens, C., Starkschall, G., et al. (2008). Use of three-dimensional (3D) optical flow method in mapping 3D anatomic structure and tumor contours across four-dimensional computed tomography data. *J Appl Clin Med Phys , 9* (1), 2738.

Zhang, T., Jeraj, R., Keller, H., Lu, W., Olivera, G., McNutt, T., et al. (2004). Treatment plan optimization incorporating respiratory motion. *Medical Physics , 31* (6), 1576-1586.